The Astrophysical Journal, 685:1005–1025, 2008 October 1

SPITZER IRAC AND MIPS IMAGING OF CLUSTERS AND OUTFLOWS IN NINE HIGH-MASS STAR FORMING REGIONS

Keping Qiu,[1,2] Qizhou Zhang,[2] S. Thomas Megeath,[3] Robert A. Gutermuth,[2] Henrik Beuther,[4] Debra S. Shepherd,[5] T. K. Sridharan,[2] L. Testi,[6,7] and C. G. De Pree[8]

Received 2007 November 19; accepted 2008 June 11

ABSTRACT

We present *Spitzer Space Telescope* IRAC and MIPS observations toward a sample of nine high-mass star forming regions at a distance of around 2 kpc. Based on IRAC and MIPS 24 μm photometric results and 2MASS JHK_s data, we carry out a census of young stellar objects (YSOs) in a $5' \times 5'$ field toward each region. Toward seven out of the nine regions, we detect parsec-sized clusters with around 20 YSOs surrounded by a more extended and sparse distribution of young stars and protostars. For the other two regions, IRAS 20126+4104 and IRAS 22172+5549, the former has the lowest number of YSOs in the sample and shows no obvious cluster, and the latter appears to be part of a larger, potentially more evolved cluster. The deep IRAC imaging reveals at least 12 outflows in eight out of the nine regions, with nine outflows prominent in the 4.5 μm band most probably attributed to shocked H_2 emission, two outflows dominated by scattered light in the 3.6 and 4.5 μm bands, and one outflow standing out from its hydrocarbon emission in the 8.0 μm band. In comparison with previous ground-based observations, our IRAC observations reveal new outflow structures in five regions. The dramatically different morphologies of detected outflows can be tentatively interpreted in terms of possible evolution of massive outflows. The driving sources of these outflows are deeply embedded in dense dusty cores revealed by previous millimeter interferometric observations. We detect infrared counterparts of these dusty cores in the IRAC or MIPS 24 μm bands. Reflection nebulae dominated by the emission from UV-heated hydrocarbons in the 8 μm band can be found in most regions and they may imply the presence of young B stars.

Subject headings: infrared: stars — ISM: jets and outflows — reflection nebulae — stars: formation — stars: pre–main-sequence

Online material: machine-readable table

1. INTRODUCTION

It is well known that high-mass stars form in dense clusters (Lada & Lada 2003). The research on embedded young clusters around young intermediate- to high-mass stars has advanced significantly via near-infrared surveys (e.g., Testi et al. 1999; Gutermuth et al. 2005; Kumar et al. 2006). The *Spitzer Space Telescope* with its unprecedented sensitivity at mid-infrared wavelengths provides a new means for identifying young stellar objects (YSOs) in star-forming regions through detection of dusty disks and envelopes. High sensitivity in the 3–24 μm bands is invaluable for distinguishing young stars from reddened background stars through infrared excess arising from circumstellar materials (Allen et al. 2004; Megeath et al. 2004; Whitney et al. 2004; Gutermuth et al. 2004; Muzerolle et al. 2004). This capability is particularly valuable for studies of high-mass star forming regions for two reasons: (1) such regions are typically located near the Galactic plane where the density of background stars is high and (2) the member YSOs are often faint due to the large distances to these regions (>1 kpc). The faint magnitude of the YSOs complicates not only the detection of members but also their identification since the density of background stars rises rapidly with increasing magnitudes. With the Infrared Array Camera (IRAC) and Multiband Imaging Photometer for *Spitzer* (MIPS), a significant census of YSOs can be carried out, which provides a fossil record of the distribution of star formation sites and information on the environments in which stars and planets form. This method is particularly effective for finding extended, lower density distributions of stars surrounding the dense regions of embedded clusters.

Extended structures, such as reflection nebulae and outflows, can also be mapped with the IRAC. Outflows emanating from the central young stars or protostars are usually detectable in rotational transitions of CO and other molecules at (sub)millimeter wavelengths. In IRAC observations, outflows can be revealed from shocked H_2 emission. Hydrodynamic simulations of shock models predict that H_2 emission is particularly strong in the 4.5 μm band (Smith & Rosen 2005). Since the 4.5 μm band is relatively free of the emission from hydrocarbons (probably in the form of polycyclic aromatic hydrocarbons, or PAHs) compared with the other three bands, and the 5.8 and 8.0 μm bands are significantly less sensitive than the shorter wavelength bands, composite images with emission from different bands coded in different colors can be a diagnostic tool for H_2 emission in outflows. A remarkable example of such a detection can be found in the IRAC observations of the HH 46/47 outflow, a collimated bipolar outflow emanating from a low-mass protostar, where the southwestern lobe was clearly seen in the 4.5 μm band as a limb-brightened bow shock cavity (Raga et al. 2004; Noriega-Crespo et al. 2004b). Smith et al. (2006) reported the IRAC detection of a spectacular outflow in the high-mass star forming region DR 21

[1] Department of Astronomy, Nanjing University, Nanjing, China.
[2] Harvard-Smithsonian Center for Astrophysics, Cambridge, MA; kqiu@cfa.harvard.edu.
[3] Department of Physics and Astronomy, University of Toledo, Toledo, OH.
[4] Max Planck Institute for Astronomy, Heidelberg, Germany.
[5] National Radio Astronomical Observatory, Socorro, NM.
[6] Osservatorio Astrofisico di Arcetri, Firenze, Italy.
[7] ESO, Karl-Schwarzschild-Strasse 2, D-85748 Garching bei München, Germany.
[8] Department of Physics and Astronomy, Agnes Scott College, Decatur, GA.

TABLE 1
SUMMARY OF THE SAMPLE

SOURCE NAME	REFERENCE CENTER (J2000.0) R.A.	REFERENCE CENTER (J2000.0) Decl.	*IRAS* LUMINOSITY ($L_\odot$)	DISTANCE (kpc)	NUMBER OF IDENTIFIED YSOs
AFGL 5142	05 30 48.00	+33 47 53.8	$10^{3.4}$	1.8	44
IRAS 05358+3543	05 39 12.78	+35 45 50.6	$10^{3.8}$	1.8	30
G192.16−3.82	05 58 13.52	+16 31 58.3	$10^{3.4}$	2.0	31
HH 80-81	18 19 12.09	−20 47 30.9	$10^{4.2}$	1.7	48
IRAS 19410+2336	19 43 11.00	+23 44 35.0	$10^{4.0}$	2.1	46
IRAS 20126+4104	20 14 26.00	+41 13 32.0	$10^{4.0}$	1.7	19
IRAS 20293+3952	20 31 10.70	+40 03 10.0	$10^{3.8}$	2.0	31
W75N	20 38 36.45	+42 37 34.0	$10^{5.1}$	2.0	77
IRAS 22172+5549	22 19 08.60	+56 05 02.0	$10^{3.3}$	2.4	91

by virtue of its brightness in the 4.5 μm band. Further investigations of the *ISO* SWS spectra of the DR 21 outflow verified that the H_2 lines contribute significantly to all four IRAC bands and the emission in the 4.5 μm band is mostly attributed to the H_2 $v = 0$–0 $S(9)$ (4.695 μm) line. Outflow activities can also be revealed from scattered light in the IRAC bands. By comparison of the deep IRAC imaging of L1448 with the radiative transfer modeling, Tobin et al. (2007) demonstrated that the observed infrared emission in the IRAC bands is consistent with the scattered light from the central low-mass protostars escaping the cavities carved by molecular outflows. Velusamy et al. (2007) reprocessed the IRAC observations of the HH 46/47 outflow using a deconvolution algorithm and found a wide-angle biconical component in scattered light in addition to the previously reported bow shock cavity. Finally, in some cases hydrocarbon emission is visible from outflow cavities, presumably due to the illumination of the cavity walls by UV radiation from the central source (van den Ancker et al. 2000).

We have observed a sample of nine high-mass star forming regions with the IRAC and MIPS instruments (PID: 3528, PI: Qizhou Zhang). These regions were chosen according to the following criteria: (1) already imaged with millimeter interferometers; (2) known to have molecular outflows; (3) outside of the GLIMPSE survey except IRAS 19410+2336; and (4) at a distance of <2.5 kpc (<5000 AU at the resolution of IRAC). These regions exhibit far-infrared luminosities ranging from 10^3 to 10^5 $L_\odot$ (see Table 1 for source parameters). We carry out a census of YSOs toward each region, and simultaneously zoom in on the central massive star formation sites with the aim of searching for infrared counterparts of millimeter continuum sources and infrared emission from outflows. In this paper we present initial results of the observations. In § 2 we describe the observations. We present observational results in § 3 and subsequent discussion in § 4. A brief summary is given in § 5.

2. OBSERVATIONS AND DATA REDUCTION

The IRAC (Fazio et al. 2004) observations were obtained from 2005 February to September except IRAS 19410+2336, which was observed in 2004 October. Each region was observed in the High Dynamic Range mode with 0.4 and 10.4 s integration times per dither, and 16 dithers per map position. The area covered by all four bands is roughly $5' \times 5'$. The total effective integration time per pixel is 166.4 s. The 0.4 s integration frames were used to obtain photometry for bright sources. The frames were processed by the *Spitzer* Science Center (SSC) using the standard pipeline version S13.2 to produce the standard Basic Calibrated Data (BCD) products. Additional bright source artifacts ("jailbar," "pulldown," "muxbleed," and "banding") were removed or mitigated using customized IDL scripts developed by the IRAC instrument team (Hora et al. 2004; Pipher et al. 2004). There are often "bandwidth" artifacts in the 5.8 and 8.0 μm images, where a decaying trail of the 4th, 8th, and in some cases even 12th pixels to the right of a bright or saturated spot is found. Currently there is no correction for this effect. Mosaics were created at the native instrument resolution of $1.2''$ pixel^{-1} from the BCD frames using Gutermuth's WCSmosaic IDL package (Gutermuth et al. 2008). Since the IRAC data are undersampled and the point-spread function (PSF) varies in shape with position and signal, aperture photometry is currently preferred over the PSF-fitting photometry. Source finding and aperture photometry were performed using Gutermuth's IDL photometry and visualization tool PhotVis, version 1.10 (Gutermuth et al. 2004, 2008). The radii of the source aperture and the inner and outer boundaries of the sky annulus were set to $2.4''$, $2.4''$, and $7.2''$, respectively. IRAC photometry was calibrated using large-aperture measurements of several standard stars from observations obtained in flight (Reach et al. 2005). There is a ∼5% calibration uncertainty due to a position-dependent gain for point sources which is not corrected by the flat field. It is the dominant source of uncertainty in the photometry of IRAC images. Fluxes at zero mag are 280.9 Jy at 3.6 μm, 179.7 Jy at 4.5 μm, 115.0 Jy at 5.8 μm, and 64.1 Jy at 8.0 μm. Magnitudes for 1 DN s^{-1} are set to 19.455 at 3.6 μm, 18.699 at 4.5 μm, 16.498 at 5.8 μm, and 16.892 at 8.0 μm, using standard aperture corrections for the radii adopted (see Table 5.7 in IRAC Data Handbook ver. 3.0). Since regions of active star formation often have bright nebulosity in the 5.8 and 8.0 μm bands, we rejected detections with photometric uncertainties above 0.25 mag in these two bands, while for the 3.6 and 4.5 μm bands detections with uncertainties above 0.2 mag were rejected. The number of detected sources and the limiting magnitude for each band toward each region are listed in Table 2.

The MIPS (Rieke et al. 2004) observations were undertaken in the photometry mode during campaigns separated by less than 1 month from the IRAC observations with the exception of IRAS 22172+5549 (1.5 months' separation) and HH 80-81 (5 months' separation). The target sources were mapped in the 24 and 70 μm bands. The MIPS 70 μm images were severely saturated and not included in this paper. The 24 μm observations consist of 400 frames with an integration of 2.62 s per frame, resulting in a total effective integration time of 1048 s. The frames were processed by the SSC standard pipeline S16.0 for AFGL 5142, IRAS 05358+3543, and G192.16−3.82, and by pipeline S16.1 for the other regions. Mosaics were created

TABLE 2
Point-Source Detections and Limiting Magnitudes

	3.6 μm		4.5 μm		5.8 μm		8.0 μm		24 μm	
Source Name	Number	Limiting Mag	Number	Limiting Mag	Number	Limiting Mag	Number	Limiting Mag	Number	Limiting Mag
AFGL 5142	517	18.206 ± 0.166	545	17.790 ± 0.168	193	15.849 ± 0.170	128	15.073 ± 0.215	16	9.774 ± 0.131
IRAS 05358+3543	377	17.674 ± 0.120	410	17.522 ± 0.185	122	15.168 ± 0.187	76	13.973 ± 0.124	12	8.386 ± 0.148
G192.16−3.82	432	18.365 ± 0.158	449	17.788 ± 0.156	130	15.640 ± 0.199	75	15.271 ± 0.200	14	9.850 ± 0.084
HH 80-81	783	16.529 ± 0.129	862	16.057 ± 0.193	578	15.066 ± 0.217	402	13.930 ± 0.239	17	7.821 ± 0.184
IRAS 19410+2336	750	16.385 ± 0.127	844	16.181 ± 0.119	411	14.807 ± 0.181	203	13.849 ± 0.216	21	7.396 ± 0.067
IRAS 20126+4104	630	17.070 ± 0.146	808	16.942 ± 0.155	253	15.894 ± 0.241	154	14.807 ± 0.196	7	7.834 ± 0.174
IRAS 20293+3952	646	16.977 ± 0.130	769	16.609 ± 0.159	282	14.953 ± 0.198	137	13.417 ± 0.159	11	7.932 ± 0.133
W75N	627	17.077 ± 0.140	798	16.869 ± 0.194	227	14.371 ± 0.235	115	12.732 ± 0.208	11	7.894 ± 0.144
IRAS 22172+5549	713	17.408 ± 0.085	869	17.053 ± 0.107	355	15.975 ± 0.238	250	15.248 ± 0.196	19	8.345 ± 0.093

based on the BCD frames using the SSC MOPEX package, with a pixel size of 1.225″ (half of the native instrument resolution). The central brightest sources in all the regions except IRAS 22172+5549 were significantly saturated. Unsaturated point sources with peaks more than 10 times the rms noise level were identified using PhotVis 1.10. Aperture photometry with a 5 pixel aperture and a sky annulus from 12 to 15 pixels was performed on these sources. Multiplying by $\frac{1}{4}$ to correct for the smaller mosaic pixels and by 1.708 to correct from a 5 pixel aperture to infinite, and using a zero mag flux of 7.3 Jy, the aperture photometry was converted to magnitudes (Winston et al. 2007). The detections with photometric uncertainties above 0.25 mag were rejected. The number of detected sources and the limiting magnitude toward each region are listed in Table 2.

The PSF-fitting photometry is preferred in crowded fields with multiple point sources. While in our MIPS 24 μm images, only about 10–20 unsaturated objects were detected in each field with a sparse distribution, and in some fields the PSF-fitting photometry is limited by the lack of ideal PSF-generating stars which are supposed to be bright, unsaturated, and uncontaminated by nebulosity. To further evaluate the aperture photometry quantitatively, we performed PSF-fitting photometry on all the 24 μm detections using the IDL DAOPHOT package. The reference PSF was generated from one to two objects chosen from the available in the field to be most suitable for PSF-generating. We then compared the returns from the PSF-fitting with the aperture photometry and found that the majority of unsaturated objects agree with each other in 0.2 mag; a few objects show differences of 0.3–0.4 mag but these objects are relatively faint and located in a spatially varying background; thus the differences are probably due to background subtraction, a limitation to both aperture and PSF-fitting photometry. Therefore, in Table 3 we show the aperture photometry with the exception of four objects. These four objects are blended with a neighboring brighter object; the resulting magnitudes derived from the contaminated aperture photometry is consequently 0.5–0.6 mag brighter than those determined with the PSF-fitting photometry. We show the PSF-fitting photometry for these objects and have annotated the table to identify these objects.

In addition, there are three slightly saturated objects in our sample (annotated in Table 3); we derived their magnitudes by manually scaling the PSF, subtracting the PSF from the image, and comparing the averaged residual of the PSF wing with a sky value taken from an annulus of 12–15 pixels. The tabulated magnitudes give an averaged residual closest to the sky value. Since raising/lowering the magnitudes by 0.1 would give an averaged residual distinctly higher/lower than the sky value, we adopt an uncertainty of 0.1 mag for these objects.

3. RESULTS

3.1. *Young Stellar Object Census*

In this section, we carry out a census of YSOs and classify them using their positions in near- to mid-infrared color-color diagrams. The results of this analysis are shown in Figure 1, where we display the colors of the detected YSOs in all nine regions, and Figure 2, where we show color-composite images of the regions with the identified YSOs overlaid. We list the number of identified YSOs in Table 1, and present the multiband photometry of each YSO in Table 3.

Although the criteria we have used to identify YSOs were developed primarily for low-mass stars, we do not select sources in specific mass ranges. The census will be dominated by low-mass YSOs, but intermediate-mass YSOs, such as Herbig Ae/Be stars with disks and intermediate-mass protostars, may be identified by the same method. Since we are observing high-mass star forming regions, high-mass young stars and protostars certainly exist in our fields. Candidate massive protostellar objects in the IRAC bands have been identified with the GLIMPSE survey (Kumar & Grave 2007); however, the colors of those objects are less well understood. It is unclear whether this method is effective for identifying high-mass stars with disks or envelopes. In our sample, there are 12 objects exhibiting obvious infrared excess in one or more color-color diagrams and also showing evidence of being an intermediate- to high-mass star (labeled as "High" in the last column of Table 3 and marked with blue crosses in Fig. 2). These objects show no or weak dust emission in the millimeter continuum (except the exciting star of the H II region W75N(A), which is within a warm dust shell) and appear very bright in near-infrared, suggesting the lack of dense envelopes thus more evolved than typical protostars. Part of these objects are identified as candidate exciting sources of the surrounding UV-heated reflection nebulae (§ 3.3). In contrast, the youngest high-mass stars in our sample are still deeply embedded in dense dusty cores which were identified as millimeter continuum sources in previous interferometric observations. Most of these millimeter sources are not detected shortward of 3.6 μm, and in some cases even undetectable at longer wavelengths. Given the extra level of complication and uncertainty in identifying and classifying these youngest high-mass objects, we exclude these objects from this section and discuss them in more detail in § 3.2.

3.1.1. *IRAC Diagram*

Allen et al. (2004) and Megeath et al. (2004) have established a YSO classification scheme in the IRAC color-color diagram [3.6] − [4.5] versus [5.8] − [8.0]. This scheme was confirmed

TABLE 3
YSOs: 2MASS, IRAC, MIPS 24 μm Photometry

R.A.[a]	Decl.[a]	J	H	K_s	[3.6]	[4.5]	[5.8]	[8.0]	[24][b]	Remarks[c]
					AFGL 5142					
05 30 36.61	+33 49 18.9	...	...	...	14.945 ± 0.013	14.597 ± 0.015	14.330 ± 0.051	13.522 ± 0.073	...	II
05 30 36.79	+33 47 18.7	...	...	...	14.672 ± 0.014	14.345 ± 0.011	13.975 ± 0.053	13.331 ± 0.046	...	II
05 30 37.98	+33 49 02.2	...	...	...	11.907 ± 0.006	11.530 ± 0.005	11.264 ± 0.006	10.540 ± 0.021	7.149 ± 0.021	II
05 30 40.18	+33 46 18.2	...	...	...	15.257 ± 0.016	14.343 ± 0.011	13.485 ± 0.029	12.623 ± 0.029	9.156 ± 0.073	I
05 30 42.14	+33 48 32.8	...	...	...	15.162 ± 0.035	14.426 ± 0.036	13.428 ± 0.060	12.624 ± 0.061	...	II
05 30 42.36	+33 48 15.1	12.523 ± 0.023	11.502 ± 0.022	10.905 ± 0.019	9.896 ± 0.002	9.407 ± 0.002	8.877 ± 0.002	8.064 ± 0.002	4.982 ± 0.035	II
05 30 42.67	+33 48 59.7	...	...	...	14.783 ± 0.012	14.573 ± 0.015	14.510 ± 0.067	14.011 ± 0.099	...	II
05 30 43.39	+33 46 00.8	...	...	...	13.813 ± 0.014	13.143 ± 0.014	12.439 ± 0.019	11.216 ± 0.012	7.356 ± 0.021	I
05 30 45.26	+33 48 26.9	...	...	...	14.450 ± 0.031	13.467 ± 0.021	12.687 ± 0.103	11.950 ± 0.175	...	I
05 30 46.06	+33 47 54.2	12.467 ± 0.026	11.303 ± 0.026	10.350 ± 0.022	8.462 ± 0.014	7.806 ± 0.010	5.900 ± 0.024	4.010 ± 0.032	$\ll$ 0.626	High[1]

Notes.—Table 3 is published in its entirety in the electronic edition of the *Astrophysical Journal*. A portion is shown here for guidance regarding its form and content. A filled triangle indicates that this is most likely attributed to the millimeter source(s) in Zhang et al. (2007). A star symbol indicates that this is blended with a neighboring brighter object in the MIPS 24 μm band; magnitudes are derived from the PSF-fitting photometry. A double-star symbol indicates that this is slightly saturated in the MIPS 24 μm band; magnitudes are derived by manually scaling the PSF, subtracting the PSF from the image, and comparing the residual of the PSF wing with a sky value. Additional notes about the sources as follows: (1) the exciting source of the surrounding reflection nebula, associated with the luminous *IRAS* source (Hunter et al. 1995), a B2 star at 3 Myr from its position in the J vs. $J - H$ diagram (Chen et al. 2005); (2) the exciting source of the surrounding reflection nebula, coincident with the *IRAS* 12 μm emission peak, a candidate Herbig Ae/Be star suggested by Porras et al. (2000); (3) the exciting source of the surrounding reflection nebula, spectral type of B2–B3 estimated from the centimeter free-free emission observed by Martí et al. (1993); (4) an intermediate- to high-mass pre–main-sequence star suggested by Aspin & Geballe (1992); (5) the exciting source of the surrounding reflection nebula, spectral type of B2–B3 estimated from the centimeter free-free emission observed by Martí et al. (1993), an intermediate- to high-mass pre–main-sequence star suggested by Aspin & Geballe (1992); (6) the exciting source of the surrounding reflection nebula; (7) an intermediate-mass YSO suggested by Palau et al. (2007); (8) the exciting source of the surrounding reflection nebula, a young B1 star surrounded by a relatively extended UC H II region (Palau et al. 2007); (9) a young B star with a 1–20 μm luminosity of 254 $L_\odot$ (Persi et al. 2006) to 540 $L_\odot$ (Moore et al. 1991); (10) the exciting source of the surrounding reflection nebula, a B0.5 star at 1–5 Myr surrounded by the expanding H II region W75N(A) and within a warm dust shell (Haschick et al. 1981; Shepherd et al. 2003, 2004b); (11) a young intermediate-mass star with a 1–20 μm luminosity of 36 $L_\odot$ (Persi et al. 2006); (12) the exciting source of the surrounding reflection nebula.

[a] J2000.0 coordinates.

[b] Sources significantly saturated in the MIPS 24 μm band are marked with the photometry of $\ll$0.626, implying a flux level much higher than the saturation limit of 4.1 Jy.

[c] I = protostars; II = Class II; I/II = Class I/II; IRe = YSOs only identifiable in the 2MASS-IRAC diagrams; High = candidates of intermediate- to high-mass YSOs—see notes 1–11 for details.

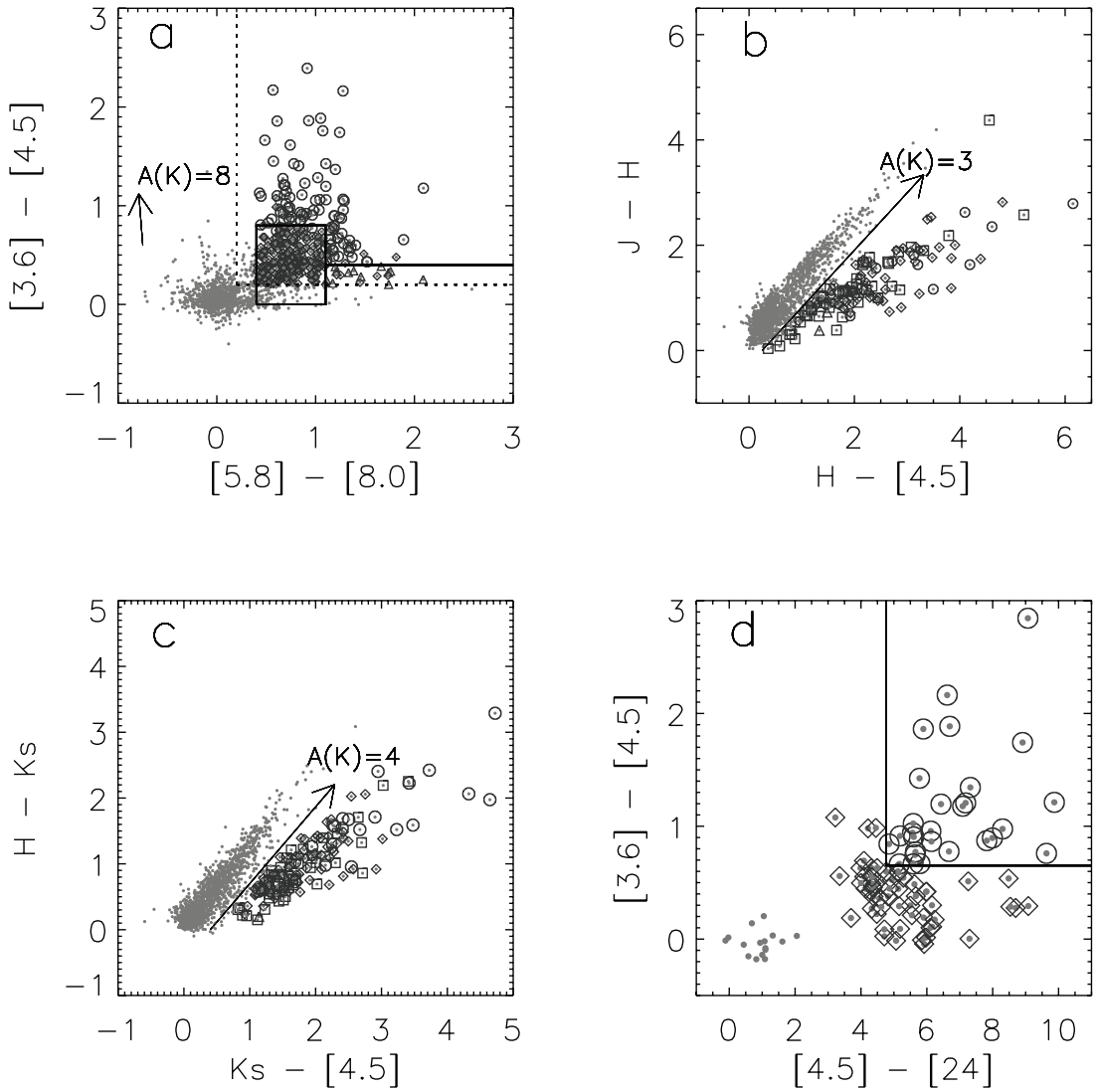

FIG. 1.—Color-color diagrams used to identify and classify YSOs. Protostars, Class I/II, and Class II objects are encircled with circles, triangles, and diamonds, respectively. YSOs that can only be identified in the IRAC-2MASS diagrams are encircled with squares. Arrows in the first three diagrams are reddening vectors derived from an averaged reddening law in nearby star-forming regions (Flaherty et al. 2007). (*a*) The IRAC diagram. The rectangle marks the Class II region determined by Allen et al. (2004) and Megeath et al. (2004). The vertical and horizontal dotted lines represent the requirements of $[5.8] - [8.0] > 0.2$ and $[3.6] - [4.5] > 0.2$, respectively. The horizontal solid line to the right of the Class II rectangle labels the criterion of $[3.6] - [4.5] = 0.4$ and $[5.8] - [8.0] > 1.1$, which is used to distinguish between protostars and Class I/II objects (Megeath et al. 2004). (*b*, *c*) IRAC-2MASS diagrams. Sources more than 1 σ to the right of the reddening vectors are identified as having intrinsic infrared excesses. (*d*) The IRAC-MIPS diagram. The outlined region in the upper right corner represents the protostar region. An isolated group of sources in the lower left of the diagram are recognized as Class III/field stars. Objects located outside of the protostar region and not in the Class III/field stars group are classified as Class II.

by Hartmann et al. (2005) with an IRAC survey of a sample of known Taurus pre–main-sequence stars, even though some ambiguities were found in a few cases. Here we adopt this scheme to classify YSOs detected in all four IRAC bands. The $[5.8] - [8.0]$ color is insensitive to reddening and is effective at distinguishing between highly reddened background stars with photospheric emission only and young stars with circumstellar material. Thus we require $[5.8] - [8.0] > 0.2$ for all the identified YSOs. Bright nebulosity dominated by hydrocarbon emission features can be found in all the regions and has a very red $[5.8] - [8.0]$ color.

To assess the impact of nebulosity on creating false detections, we added artificial stars to each of the mosaics. Each artificial star was 10 pixels (12″) to the west of an actual source that was detected in the 3.6 and 4.5 μm bands, and the magnitude of the artificial star in all four IRAC bands was set to the 3.6 μm magnitude of the actual source. Thus, the artificial stars had $[3.6] - [4.5]$ and $[5.8] - [8.0]$ colors equal to 0. These sources accurately sampled the range of magnitudes and background nebulosities found in the image. We then recovered the photometry to determine how many such stars would be mistaken as having infrared excesses due to the nebulosity. Although there were about 10–30 sources with $[5.8] - [8.0] > 0.2$, only 1–3 of the sources had a color of $[3.6] - [4.5] > 0.2$.

Hence we require $[3.6] - [4.5] > 0.2$ to eliminate pure photospheres contaminated by hydrocarbon emission nebulosity. Figure 1*a* shows the $[3.6] - [4.5]$ versus $[5.8] - [8.0]$ diagram for objects merged from all nine regions and detectable in all four IRAC bands. In this diagram, objects with $0.2 < [3.6] - [4.5] < 0.8$ and $0.4 < [5.8] - [8.0] < 1.1$ are classified as Class II; objects with $[3.6] - [4.5] > 0.8$ and $[5.8] - [8.0] > 0.2$, or $[3.6] - [4.5] \geq 0.4$ and $[5.8] - [8.0] > 1.1$, are classified as protostars (including Class 0 and Class I objects); while objects with $[5.8] - [8.0] > 1.1$, which is consistent with that of protostars, but with $0.2 < [3.6] - [4.5] < 0.4$, which is lower than that of

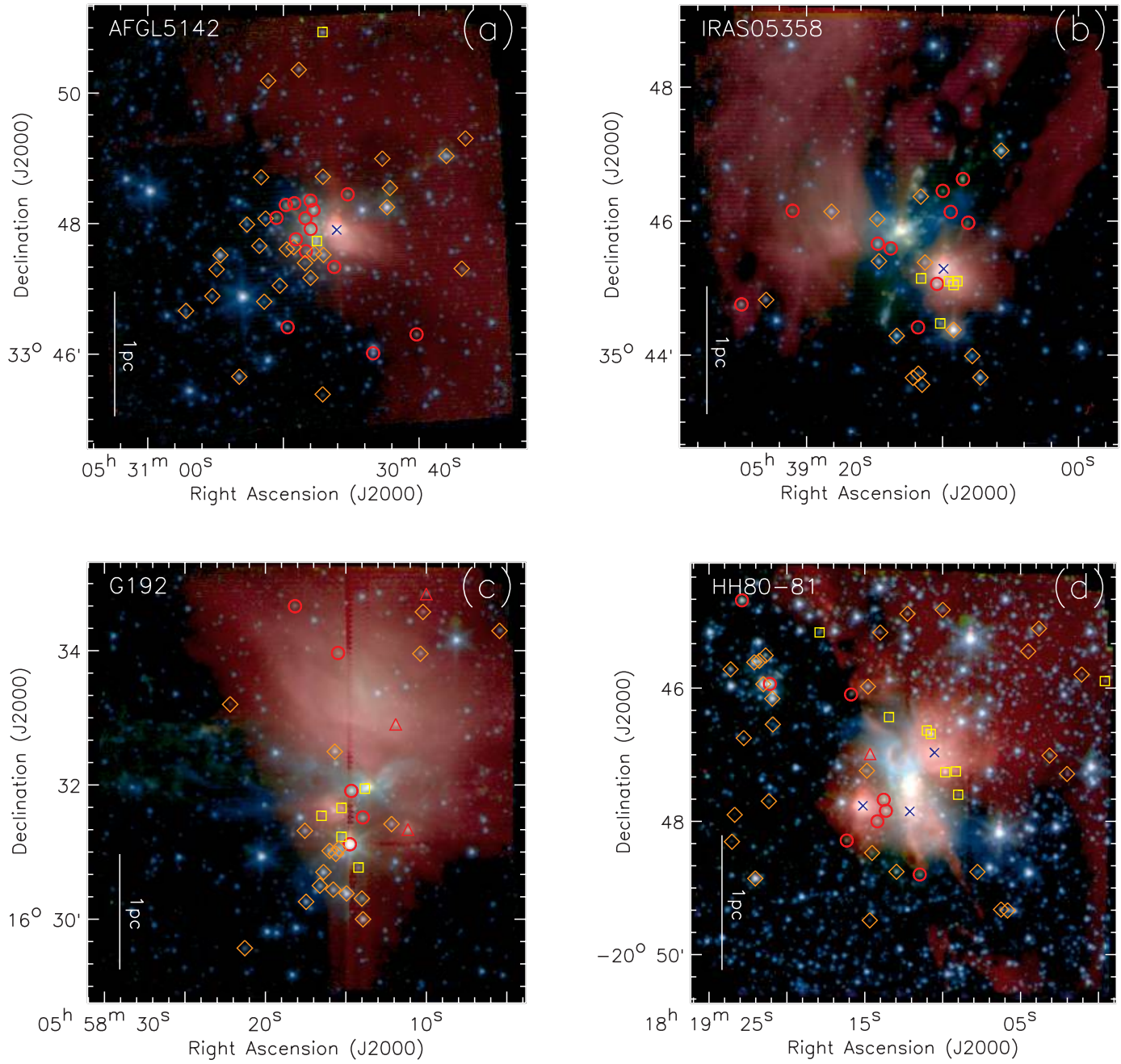

FIG. 2.—IRAC 3.6/4.5/8.0 μm (*blue*/*green*/*red*) three-color composite images of all nine regions. Red circles, red triangles, and brown diamonds represent protostars, Class I/II, and Class II objects, respectively. Yellow squares mark YSOs that can only be identified in the IRAC-2MASS diagrams. Blue crosses label candidates of intermediate- to high-mass young stars (see "high" sources in Table 3 for details).

protostars, are classified as Class I/II. For those detected in the 24 μm band, we reexamine them in the IRAC-MIPS diagram.

From both observations and model calculations, the [3.6] − [4.5] versus [5.8] − [8.0] diagram has been proven quite effective in separating YSOs with dusty disks or envelops from purely photospheric emission stars (Hartmann et al. 2005; Robitaille et al. 2006). The principal ambiguity for the [3.6] − [4.5] versus [5.8] − [8.0] classification scheme lies in distinguishing protostars from Class II objects. From the direction of the reddening vector in Figure 1*a*, the identified protostars immediately above the Class II rectangle ($0.8 \lesssim [3.6] - [4.5] \lesssim 1.2$) are likely reddened Class II objects. In addition, some of the objects immediately to the right of the Class II rectangle ($1.1 \lesssim [5.8] - [8.0] \lesssim 1.5$), which are identified as protostars or Class I/II, are likely Class II objects contaminated by hydrocarbon emission. In addition, some intrinsic characteristics of YSOs make the classification ambiguous as well. For example, geometric effects including bipolar outflow cavities, flattened patterns of envelopes, and pole-on geometry will all make the IRAC colors of protostars much bluer (Hartmann et al. 2005; Robitaille et al. 2006). In a few cases the discrimination between Class II objects and Class III/field stars is also ambiguous; some YSOs with circumstellar disks have an evacuated or very optically thin inner hole and show little infrared excess shortward of 8.0 μm, and then can be misidentified as Class III/field stars.

3.1.2. *2MASS-IRAC Diagrams*

The IRAC 5.8 and 8.0 μm bands are far less sensitive than the 3.6 and 4.5 μm bands (see the limiting magnitudes in Table 2),

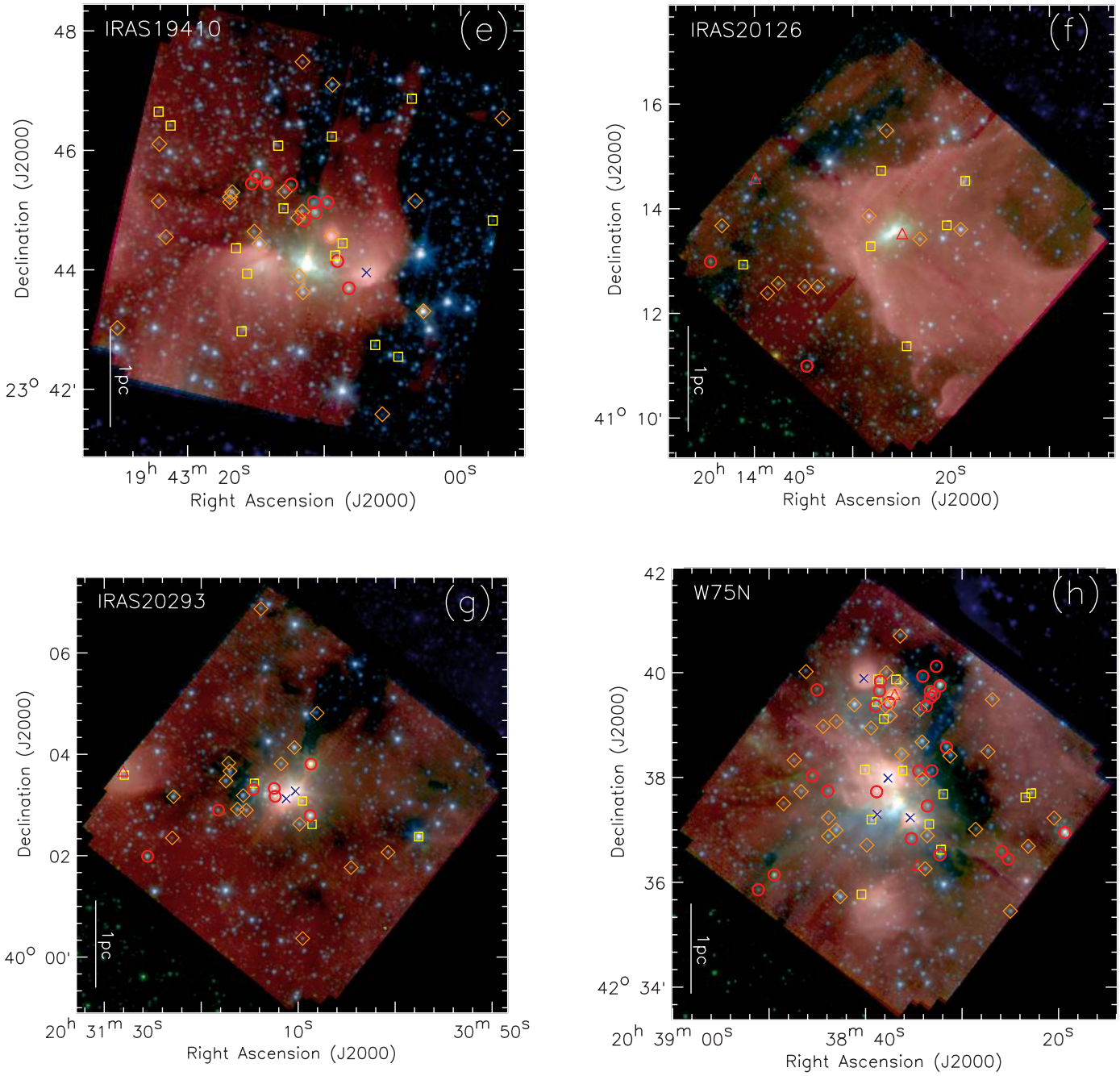

FIG. 2—*Continued*

and are often dominated by bright nebulosity in observations of active star-forming regions. For this reason, we combine the IRAC photometric results with data from the 2MASS JHK_s Point Source Catalog. We limit the JHK_s photometric uncertainty to be less than 0.1 mag. Since the 4.5 μm band is the most sensitive band to YSOs among all four IRAC bands (Gutermuth et al. 2004), we use the $J - H$ versus $H - [4.5]$ and $H - K_s$ versus $K_s - [4.5]$ diagrams (Figs. 1*b* and 1*c*) to identify objects with infrared excess emission but not detected in the IRAC longer wavelength bands. In Figures 1*b* and 1*c*, objects with the $H - [4.5]$ or $K_s - [4.5]$ colors more than 1 σ beyond the reddening vectors are identified as objects with intrinsic infrared excess. The extinction law in the mid-infrared wavelengths toward star-forming regions, in particular toward distant high-mass star forming regions, has not been well established. Most recently, Flaherty et al. (2007) derived the interstellar extinction laws in IRAC bands toward five nearby star-forming regions. We adopt the average of the extinction laws derived by Flaherty et al. for our sample. From the dispersion of the objects left to the reddening vectors in these two diagrams, it seems the adopted reddening law is applicable for our high-mass star forming regions. The positions offsets of the reddening vectors in these two diagrams, which were determined by Winston et al. (2007) for Serpens, also appear to be a good approximation for our regions. However, the completeness of the YSO identification from these two diagrams are significantly limited by the modest sensitivity of the 2MASS survey. Deeper near-infrared observations will not only improve the completeness but also help to derive a more accurate reddening law toward each region, which would improve the reliability of the YSOs identification.

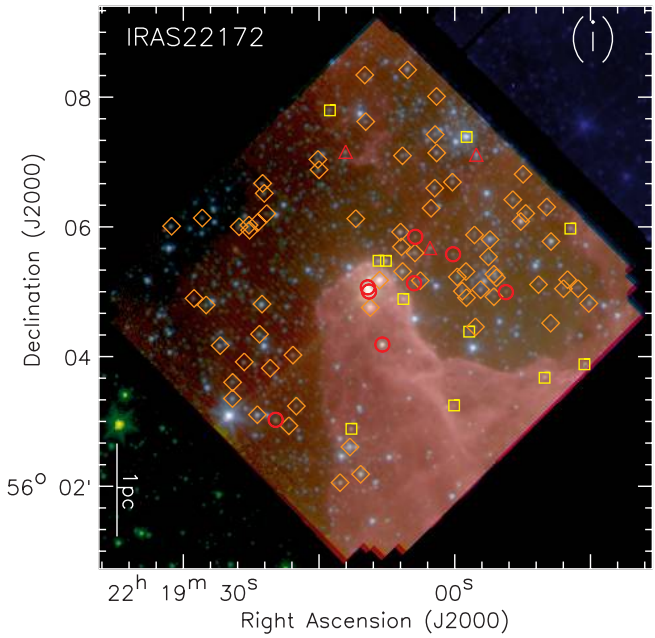

FIG. 2—*Continued*

3.1.3. *IRAC-MIPS Diagram*

Including data at wavelengths longward of 20 μm is valuable for more reliable classification of YSOs (Robitaille et al. 2006). In Figure 1*d*, we use the [3.6] − [4.5] versus [4.5] − [24] diagram to classify YSOs which are detectable both in the two most sensitive IRAC bands and in the MIPS 24 μm band. Sources with spectral indexes greater than −0.3 have IRAC-MIPS colors [3.6] − [4.5] > 0.652 and [4.5] − [24] > 4.761. These sources would include both the flat spectrum and Class I objects in the classification scheme of Greene et al. (1994). In addition, the high sensitivity of *Spitzer* data allows for the detection of previously identified Class 0 sources in the mid-infrared (Noriega-Crespo et al. 2004a; Rho et al. 2006; Hatchell et al. 2007; Winston et al. 2007); consequently, Class 0 sources can also be identified by these criteria. Since an infalling envelope is required to explain the SEDs of flat-spectrum Class I and Class 0 sources (Calvet et al. 1994; Whitney et al. 2003), we refer to the combined set of these sources as protostars. In Figure 1*d*, there is clearly an isolated group close to (0, 0). The objects in this group are Class III/field stars whose emission is dominantly from photospheres. In this diagram objects outside of the protostar region and not in the Class III/field star group are classified as Class II. There is an obvious gap between protostars/Class II objects and ClassIII/field stars, suggesting this diagram is very effective in distinguishing YSOs with circumstellar materials from purely photospheric objects. From the objects that can be classified both in the [3.6] − [4.5] versus [5.8] − [8.0] and in the [3.6] − [4.5] versus [4.5] − [24] diagrams, we find that the two classification schemes are in general consistent; otherwise we adopt the latter if there is an ambiguity. With the IRAC-MIPS diagram we also identify 15 Class II objects and 2 protostars that cannot be identified in any of the other three color-color diagrams.

3.1.4. *Removing Extragalactic Contaminants*

There are mainly two classes of extragalactic contaminants that can be misidentified as YSOs (Stern et al. 2005). One is star-forming galaxies and narrow-line active galactic nuclei (AGNs) which have growing excess at 5.8 and 8.0 μm due to hydrocarbon emission. The other is broad-line AGNs which have IRAC colors very similar to that of bona fide YSOs. Gutermuth et al. (2008) have developed a method based on the Bootes Shallow Survey data to substantially mitigate these contaminants. In this method, hydrocarbon emission sources, including galaxies and narrow-line AGNs, can be eliminated by their positions in the [4.5] − [5.8] versus [5.8] − [8.0] and [3.6] − [5.8] versus [4.5] − [8.0] diagrams, while broad-line AGNs, which are typically fainter than YSOs in the *Spitzer* bands, are identified by their positions in the [4.5] versus [4.5] − [8.0] diagram. Here we adopt this method and lower the [4.5] limit in the [4.5] versus [4.5] − [8.0] diagram by 1 mag since our regions are far more distant. To further remove AGNs, we set [3.6] < 16 for YSOs not detected in the 8.0 μm band and require [24] < 8.5 for those only identifiable in the [3.6] − [4.5] versus [4.5] − [24] diagram. We filter out a total of 11 extragalactic contaminants in all nine regions.

3.1.5. *Completeness of the Census*

Although we are undertaking deep observations toward relatively nearby high-mass star forming regions, the completeness of the YSOs census is limited by a few factors. Bright extended nebulosity in the IRAC bands can be found in all the regions, which significantly limits the point-source detection in these areas. The YSO identification from the 2MASS-IRAC diagram is limited by the modest sensitivity of the 2MASS survey, while that from the IRAC-MIPS diagram suffers from the significant saturation in the MIPS 24 μm image caused by the central luminous sources. To further evaluate the completeness of the census quantitatively, we plot histograms of the sources which are counted within 0.5 mag bins of the 3.6 μm photometry in Figure 3. In this plot, all the 3.6 μm detections with signal-to-noise ratios sufficient to be identified by our point-source filter are plotted with the gray solid lines, and sources with corresponding multiband photometry so that they can be placed on one or more color-color diagrams for an assessment of infrared excess are plotted with the dark dashed lines. The identified YSO members are also

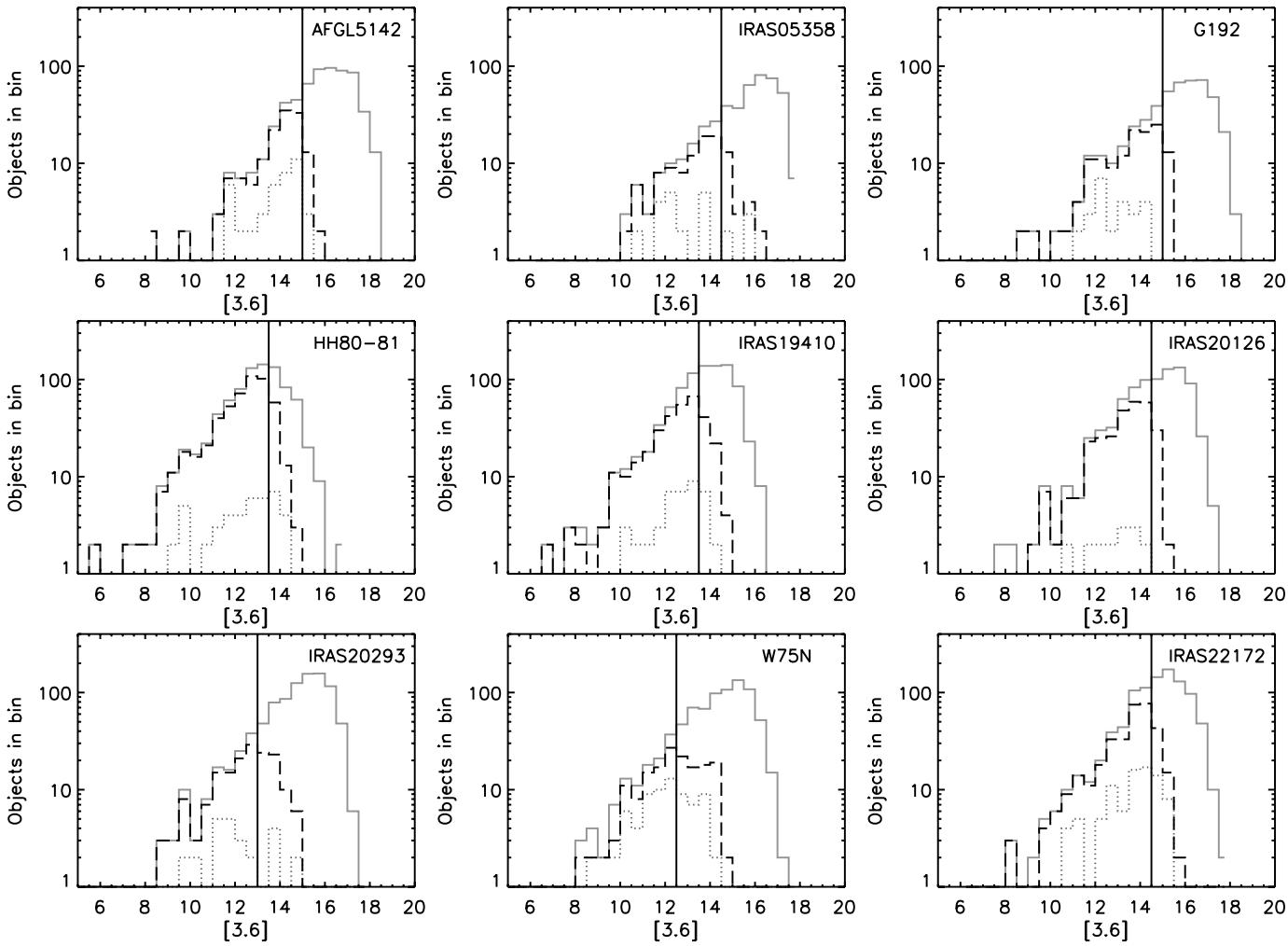

FIG. 3.—Histograms of sources in the 0.5 mag bins as a function of the 3.6 μm magnitudes. The gray solid lines plot all the 3.6 μm detections in each field. The dark dashed lines show sources with multiband photometry, which can be placed on one or more color-color diagrams for search of infrared excess. The gray dotted lines represent sources that are identified as YSOs.

plotted with the gray dotted lines. There are two types of completeness in this diagram. The first is the completeness in the 3.6 μm band, which declines strongly where a peak is evident in the solid gray line histogram. The second is the coupled multiband completeness to infrared excess sources, which is approximately given where the dark dashed line diverges from the solid gray line. Since the 3.6 μm band detects sources of fainter magnitudes than the other bands, we define the completeness magnitude as the point where the multiband histogram declines more than 30% with respect to the 3.6 μm histogram. A vertical dash-dotted line in each plot indicates the completeness magnitude. For sources with the 3.6 μm photometry brighter than the completeness magnitude, we calculate the ratio of the number of sources that can be placed on one or more color-color diagrams for the search of infrared excess to the number of the total detections (Table 4). The actual completeness to infrared excess sources is presumably higher since they will have stronger emission in the IRAC bands than field stars and young stars without disks.

3.2. *Central Massive Star Formation Sites*

Previous interferometric studies have identified dusty cores at the center of each region through the millimeter continuum emission, and so far five regions show multiple or a cluster of dusty cores. Of these millimeter sources, the deep IRAC imaging detects six at 8.0 μm, five at 5.8 μm, three at 4.5 μm, and two at 3.6 μm. The low detection rate is consistent with the deep IRAC observations of the other two nearby (1.7 kpc) high-mass star forming regions, NGC 6334I and NGC 6334I(N), where only

TABLE 4
COMPLETENESS ESTIMATES

Source Name	[3.6][a]	Completeness[b] (%)
AFGL 5142	15	84
IRAS 05358+3543	14.5	79
G192.16−3.82	15	81
HH 80-81	13.5	84
IRAS 19410+2336	13.5	73
IRAS 20126+4104	14.5	73
IRAS 20293+3952	13	85
W75N	12.5	75
IRAS 22172+5549	14.5	76

[a] Completeness magnitudes at 3.6 μm derived from Fig. 3.
[b] For sources with the 3.6 μm photometry brighter than the completeness magnitude, the fraction of the sources that can be placed on one or more color-color diagrams.

TABLE 5
INFRARED COUNTERPARTS OF MILLIMETER CORES

Source	R.A. (J2000.0)	Decl. (J2000.0)	[3.6]	[4.5]	[5.8]	[8.0]	[24]	References
AFGL 5142	05 30 47.94	+33 47 54.2	...	...	...	...	0.632 ± 0.005	1
IRAS 05358+3543	05 39 13.04	+35 45 51.2	...	7.582 ± 0.020	6.250 ± 0.015	5.098 ± 0.011	≪ 0.626	2, 3
G192.16−3.82	05 58 13.55	+16 31 58.2	9.063 ± 0.009	7.726 ± 0.007	6.915 ± 0.007	5.954 ± 0.014	≪ 0.626	4, 5
HH 80-81	18 19 12.11	-20 47 31.0	...	...	4.104 ± 0.050	3.040 ± 0.081	≪ 0.626	6
IRAS 19410+2336	19 43 11.25	+23 44 03.2	6.682 ± 0.018	4.624 ± 0.008	3.365 ± 0.004	2.780 ± 0.008	≪ 0.626	7, 8
IRAS 20126+4104	20 14 25.97	+41 13 33.1	...	...	...	5.422 ± 0.060	≪ 0.626	9, 10
IRAS 20293+3952	20 31 12.92	+40 03 23.0	...	...	...	...	1.123 ± 0.021	11, 12, 13
W75N	20 38 36.49	+42 37 33.5	...	6.161 ± 0.22	4.451 ± 0.017	3.346 ± 0.018	≪ 0.626	14

REFERENCES FOR INTERFEROMETRIC MILLIMETER CONTINUUM OBSERVATIONS.—(1) Zhang et al. 2007; (2) Beuther et al. 2002; (3) Beuther et al. 2007; (4) Shepherd & Kurtz 1999; (5) Shepherd et al. 2004a; (6) Gómez et al. 2003; (7) Beuther et al. 2003; (8) Beuther & Schilke 2004a; (9) Shepherd et al. 2000; (10) Cesaroni et al. 2005; (11) Beuther et al. 2004b; (12) Beuther et al. 2004c; (13) Palau et al. 2007; (14) Shepherd 2001.

one out of eleven SMA 1.3 mm sources shows a detectable infrared counterpart (Hunter et al. 2006). Kumar & Grave (2007) suggested that the IRAC band emission of candidate massive protostellar objects arises from the luminous envelopes around the protostars rather than their photospheres or disks. In our sample, the number of detected infrared counterparts increases with the increasing wavelength of the band, despite the fact that the 3.6 and 4.5 μm bands are much more sensitive than the 5.8 and 8.0 μm bands. This implies a steeply rising SED in the IRAC bands, which is consistent with the interpretation that the emission is mostly coming from the dense envelopes. All the six millimeter sources detected in one or more IRAC bands appear significantly saturated in the MIPS 24 μm band, while there are two millimeter sources detected at 24 μm without saturation but undetectable in any of the four IRAC bands. We list the IRAC or MIPS 24 μm photometry of detected millimeter sources in Table 5. In our sample, high-mass stars deeply embedded in dusty cores are early-B types estimated from far-infrared luminosities, ionizing UV radiation fluxes (if UC H II regions are detected), and core masses. Also considering they are associated with molecular outflows indicative of active accretion, we refer to these deeply embedded B stars as proto-B stars.

In all nine regions, massive molecular outflows have been identified in millimeter lines of CO and/or SiO. In the IRAC observations, the central high-mass sources are found to be associated with extended nebulosity. Several mechanisms produce extended nebulosity in the IRAC bands. Prominent features from hydrocarbons appear in the 3.6, 5.8, and 8.0 μm bands, with the strongest emission features in the 8.0 μm band (Werner et al. 2004). Vibrational and rotational H_2 lines appear in all four bands, with the weakest and most spatially confined emission in the 3.6 μm band (Smith et al. 2006; Smith & Rosen 2005); this H_2 emission is most apparent in the 4.5 μm band due to the high sensitivity of this band and presence of strong rotational lines (Smith & Rosen 2005). Finally scattered light may also produce nebulosity which is expected to be the strongest in the 3.6 μm band. To distinguish between these different mechanisms, we employ 3.6/4.5 μm two-color and 3.6/4.5/8.0 μm three-color composite images to highlight emission from shocked H_2 in outflows, scattered light from outflow cavities, and emission from UV-heated hydrocarbons. We identify a total of 12 outflows in eight out of the nine regions. Reflection nebulae and externally heated rimmed clouds are detected as well.

In the following subsections, we discuss each region separately. For Figures 4–16, the 3.6, 4.5, and 8.0 μm emissions in color composites are coded in blue, green, and red, respectively; millimeter continuum cores from previous observations are marked

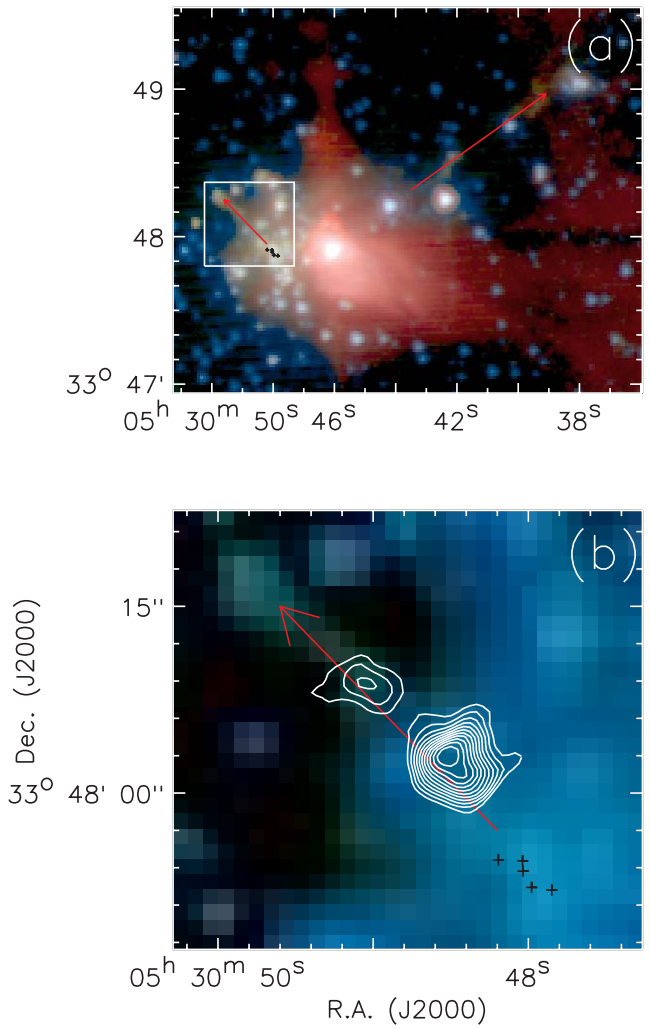

FIG. 4.—AFGL 5142. (*a*) The 3.6/4.5/8.0 μm (*blue*/*green*/*red*) three-color composite of the central part. The short and long arrows mark the orientations of two detected jets. (*b*) The 3.6/4.5 μm (*blue*/*green*) two-color composite of the area labeled by a rectangle in (*a*), to more clearly show the short jet prominent in the 4.5 μm band. Contours are high-velocity CO emission from outflow B in Zhang et al. (2007). Plus signs in both panels mark the millimeter continuum peaks (MM1–MM5) from Zhang et al. (2007).

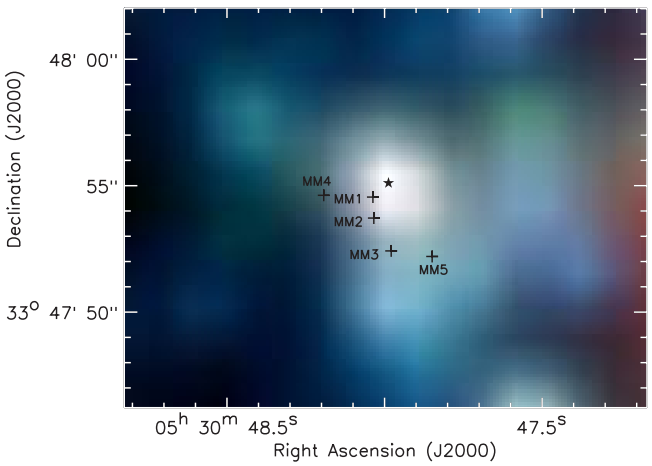

FIG. 5.—AFGL 5142: the 3.6/4.5/8.0 μm (*blue*/*green*/*red*) three-color composite of the inner massive star formation site, to show a comparison between the point-source detections in the IRAC bands and previous millimeter continuum observation. The star symbol denotes a protostar identified from the color-color diagrams. Plus signs mark the millimeter continuum peaks (MM1–MM5) from Zhang et al. (2007).

as plus signs; CO and SiO outflows from previous observations are shown in contours; additional symbols (arrows, dashed curves, etc.) are merely to highlight the IRAC outflows from the ambient reflection nebulae or scattered light.

3.2.1. *AFGL 5142*

In Figure 4*a*, a short jet in the east and a long jet in the west are detected. The short jet coincides with the axis of one of the three jetlike molecular outflows detected in the CO (2–1) and SO (6_5–5_4) with the SMA (outflow B in Zhang et al. 2007; see contours in Fig. 4*b*). The long jet, on the other hand, coincides with the axis of an extended remnant outflow detected in CO (2–1) with the CSO telescope (Hunter et al. 1995). The emission from these two jets is most prominent in the 4.5 μm band, in agreement with the previous ground-based 2.12 μm H_2 $v = 1$–0 $S(1)$ observations (Hunter et al. 1995; Chen et al. 2005). Apparently the IRAC imaging of this region reveals internal driving agents of two molecular outflows.

Toward the center of AFGL 5142, Zhang et al. (2007) detected five millimeter continuum sources (MM1–MM5 in Fig. 5). In Figure 5 a bright source residing 0.8″ northwest of MM1 (marked with a star symbol) is detected in the 2MASS K_s band, all four IRAC bands, and the MIPS 24 μm band (see the detection at $\alpha = 05^h30^m47.98^s$, $\delta = 33°47'54.9''$ [J2000.0] in Table 3). It is classified as a protostar in the [3.6] − [4.5] versus [5.8] − [8.0] and [3.6] − [4.5] versus [4.5] − [24] diagrams. The projected offset between this source and MM1 is marginally within the IRAC astrometry allowance. Thus it is still possible that this source is the infrared counterpart of MM1. However, Zhang et al. (2007) detected a forest of molecular lines toward MM1 and suggested that it is the driving source of a jetlike molecular outflow, which implies that the protostar deeply embedded in MM1 is actively accreting. Such a protostellar core is usually obscured in the *K* band (e.g., Walther et al. 1990; Aspin et al. 1991; and observations of other regions in our sample). Considering the source is detected in the 2MASS K_s band, a survey with limited sensitivity, we suggest that it is most likely a different source rather than the infrared counterpart of MM1. But the 24 μm emission can still arise from MM1 and/or other millimeter sources given its relatively low resolution (∼5″); thus we list the 24 μm photometry in Table 5. The 24 μm detection is located at the bright PSF wing of a nearby saturated source, resulting in a potential overestimate of the flux by about 0.3–0.4 Jy. The driving sources of the multiple CO/SO outflows have not been unambiguously identified. Zhang et al. (2007) suggested MM3 may be the powering source of the CO outflow coincident with the short jet in Figure 4*b*. The long jet is apparently powered by a relatively more evolved young B star (denoted by a blue cross in Fig. 2*a*).

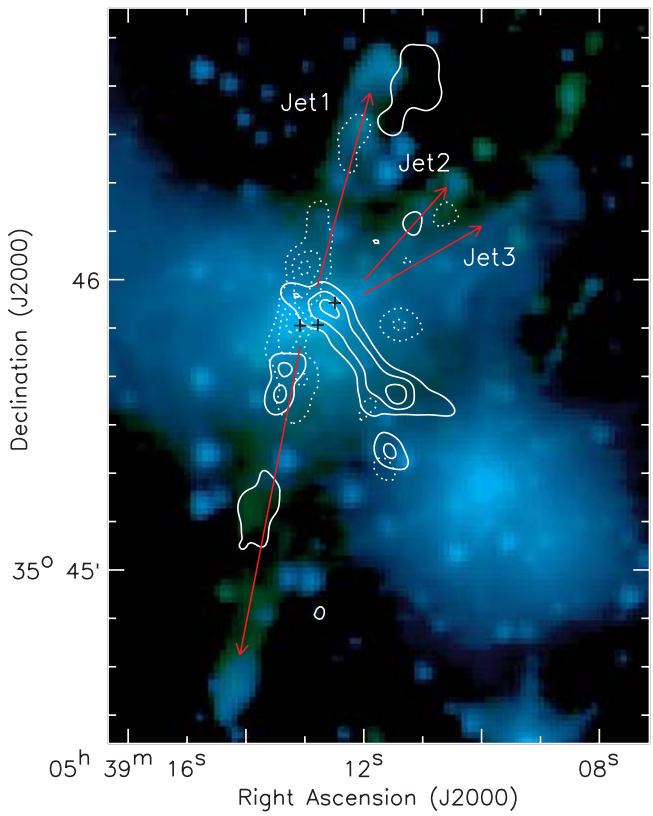

FIG. 6.—IRAS 05358: the 3.6/4.5 μm two-color composite of the central part. The arrows mark the orientations of three detected jets, which are labeled "Jet1," "Jet2," and "Jet3" from east to west. Solid and dashed contours denote blue- and redshifted CO emission from Beuther et al. (2002). Plus signs mark the 3.1 mm continuum peaks from Beuther et al. (2007).

3.2.2. *IRAS 05358+3543*

In Figure 6 three highly collimated jets emanating from a group of millimeter continuum sources are detected in the central part of IRAS 05358+3543 (hereafter referred as IRAS 05358). Jet 1 coincides with a well-collimated outflow in CO (1–0) reported by Beuther et al. (2002) (see contours in Fig. 6). Jet 2 coincides with the axis of a high-velocity CO outflow (outflow B in Beuther et al. 2002). Several knots from these two jets are almost exactly coincident with the previously identified 2.12 μm H_2 knots (Porras et al. 2000; Jiang et al. 2001; Beuther et al. 2002; Kumar et al. 2002). Beuther et al. (2002) did not report the identification of jet 3, but weak emission features coincident with this jet can be found in their 2.12 μm H_2 image. Kumar et al. (2002) suggested the existence of this jet, but the emission appears to be weaker since their H_2 observations are less deep than that of Beuther et al. (2002). In the IRAC imaging (Fig. 6), a chain of emission knots in this jet can be identified and even its tip can be identified despite the contamination by a nebulous knot. There is no reported detection of an outflow toward this jet in millimeter CO or SiO observations. However, in the northern lobe of the SiO (2–1) outflow proposed by Beuther et al. (2002, their

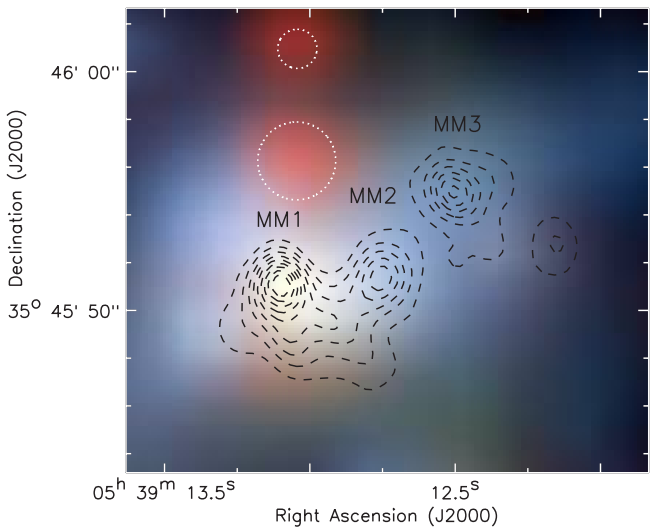

FIG. 7.—IRAS 05358: the 3.6/4.5/8.0 μm three-color composite of the inner massive star formation site, to show a comparison between the point-source detections in the IRAC bands and previous millimeter continuum observation. The dashed contours are for the 3.1 mm continuum emission with three peaks labeled "MM1," "MM2," "MM3" (Beuther et al. 2007). The two white dashed circles denote bandwidth artifacts in the 8.0 μm band.

Fig. 8*b*), the highest contours show elongation coincident with jet 3. Considering SiO is a good shock tracer at (sub)millimeter wavelengths, the elongated SiO emission could be at least partially powered by jet 3.

At the center of this region, Beuther et al. (2002, 2007) detected three millimeter continuum sources at $\sim$2″–3″ resolutions (marked as MM1–MM3 in Fig. 7). The brightest emission feature in Figure 7 coincides with MM1; two northern "red" features (denoted by two white dashed circles) are not real but "bandwidth" artifacts. An investigation of the emission in individual bands shows that emission features coincident with MM2 and MM3 are discernible in the 3.6 and 4.5 μm bands but are not identified by our point-source filter. The emission feature coincident with MM1 is marginally discernible in the 3.6 μm band, and identified as a point source longward of 4.5 μm. The MIPS 24 μm emission from this area is significantly saturated. From its extremely red IRAC colors ([4.5] − [5.8] = 1.33 and [5.8] − [8.0] = 1.15) and position coincidence with MM1, we suggest that this source is the infrared counterpart of MM1 and list its photometry in Table 5. At higher resolutions ($\lesssim$1″), the MM1 core splits into two subcores at 875 μm and 1.2 mm (Beuther et al. 2007). One of the two subcores coincides with a point source at 7.9 μm detected with the Gemini North telescope (Longmore et al. 2006). The substructure of MM1 cannot be resolved in the IRAC observations. The flux of 0.586 Jy at 8.0 μm ([8.0] = 5.098) is consistent with the flux of 0.68 Jy at 7.9 μm reported in Longmore et al. (2006), suggesting that the flux of the IRAC source is dominated by the subcore coincident with the 7.9 μm detection. MM1 (or more precisely, one of the two subcores in MM1) is suggested as the driving source of jet 1 (Beuther et al. 2007). A reliable one-to-one association between jet 2, jet 3, and any two millimeter sources in this region cannot be established with the current data.

3.2.3. *G192.16−3.82*

Shepherd et al. (1998) detected a west-east bipolar outflow in CO (1–0) in G192.16−3.82 (hereafter referred as G192). The eastern lobe of this outflow is detected in the 3.6 and 4.5 μm bands. In Figure 8 the most prominent features of this lobe are "green" nebulosities within the area outlined by two dashed lines. The emission to the west of these features is confused by the bright reflection nebula, but a "blue" V-shaped structure, with the millimeter source at the tip, is still discernible in the three-color composite of the field (Fig. 2*c*). The overall structure of the eastern lobe in the IRAC imaging, i.e., the green features as well as the V-shaped inner part, roughly coincides with but far exceeds the eastern lobe of the CO outflow. The prominence in the 4.5 μm band and coincidence with previous Hα and [S II] detections (Devine et al. 1999) strongly suggest that the green nebulosities are shock excited H_2 knots. The base of the western lobe of the CO outflow is also detected in the IRAC imaging, with the prominent feature being a candle-flame-shaped structure (delineated by a dashed curve in Fig. 8, but more prominent in Fig. 2*c*); this structure is previously detected in the *K*-band imaging (Shepherd et al. 1998; Devine et al. 1999). One interesting aspect of this outflow is that although the eastern lobe is filled with shocked H_2 knots, a collimated component cannot be found either in our IRAC imaging or previous observations. The CO outflow appears to be driven by a wide-angle wind revealed in the IRAC, Hα, and [S II] observations.

A proto-B star surrounded by an UC H II region and embedded in a dense dusty core was suggested as the driving source of the outflow (Shepherd & Kurtz 1999; Shepherd et al. 2004a). A bright source coincident with the millimeter continuum peak is

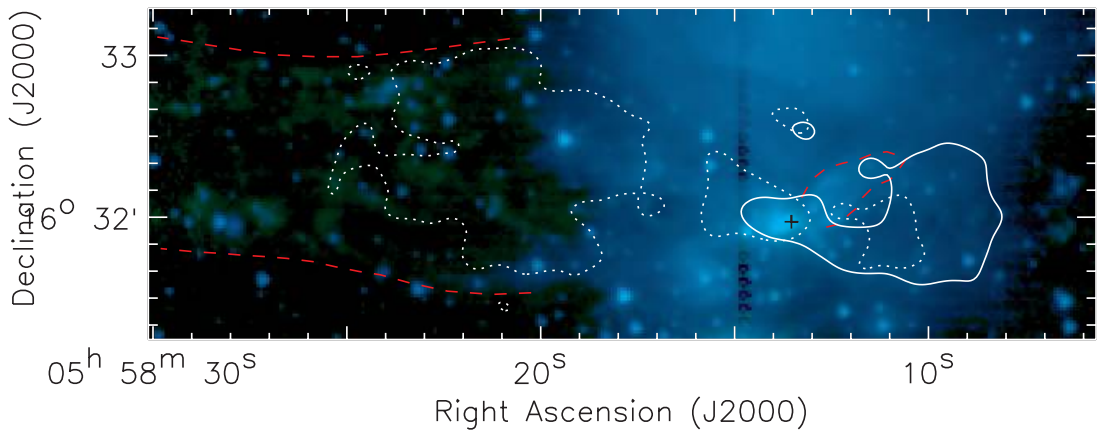

FIG. 8.—G192: the 3.6/4.5 μm two-color composite of the central part. Solid and dashed contours are the lowest contours of red- and blueshifted CO outflow, respectively (Shepherd et al. 1998). Two red dashed lines in the east outline the area filled with "green" nebulosities, and the red dashed curve in the west the candle-flame-shaped structure (this structure is more prominent in the three-color composite Fig. 2*c*). The plus sign marks the millimeter continuum peak from Shepherd et al. (1998).

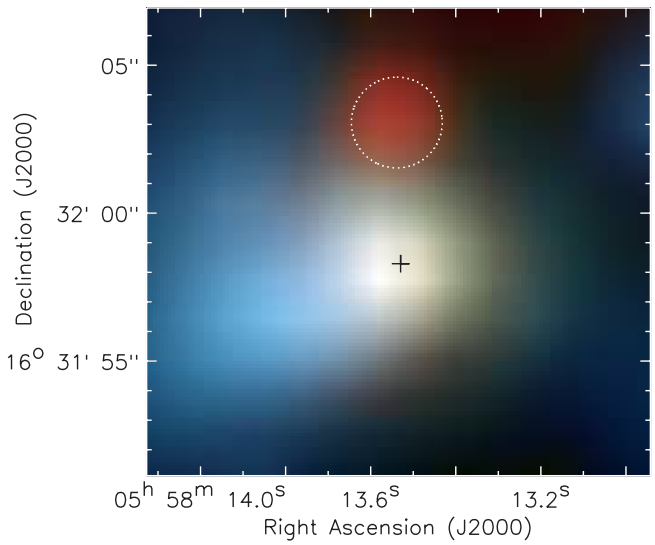

FIG. 9.—G192: the 3.6/4.5/8.0 μm three-color composite of the inner massive star formation site, to show a comparison between the point-source detections in the IRAC bands and previous millimeter continuum observation. The plus sign marks the millimeter continuum peak from Shepherd et al. (1998).

detected in the IRAC bands and shows very red IRAC colors (Fig. 9). We suggest that it is the infrared counterpart of the millimeter source and list its photometry in Table 5. A detailed comparison between the infrared and millimeter emission in the region will be presented in a future work (D. S. Shepherd et al., in preparation).

3.2.4. *HH 80-81*

An extraordinarily well-collimated and powerful radio jet was previously detected in HH 80-81 (Martí et al. 1993, 1995, 1998; see contours in Fig. 10). Having the radio jet right at the axis, the *Spitzer* data for the first time reveals a bipolar cone-shaped cavity with its emission most prominent in the 8.0 μm band with an extent of about 4 pc (Fig. 10). Low-mass protostellar outflows are often found to consist of two components, with an axial narrow jetlike component surrounded by a wide-angle biconical component (Lee et al. 2006; Palau et al. 2006). It is unclear whether outflows emanating from high-mass young stars or protostars may exhibit two components similar to low-mass outflows. Our IRAC imaging as well as previous radio continuum observations of the HH 80-81 outflow provides the best case of a two-component outflow emanating from a 10^4 $L_\odot$ source. The remarkable prominence in the 8.0 μm band suggests that the emission of the IRAC biconical structure is from hydrocarbons heated by UV photons from the central source. Single-dish observations revealed a large bipolar outflow in CO (1–0) (Yamashita et al. 1989; Benedettini et al. 2004), with the northern lobe being blueshifted and the southern lobe redshifted. The orientation of the CO outflow is roughly consistent with the IRAC outflow structure. In the three-color composite image (Fig. 2*d*), a curved structure in the northern lobe stands out in the 3.6 μm emission (*blue*). This curved structure is very bright in previous near-infrared *K*-band observations and has been suggested as the wall of a parabolic cavity (Aspin et al. 1991). The dominant 3.6 μm emission from this structure may be partly explained by the scattered light in this structure being enhanced by forward scattering and lower extinction. The 8.0 μm emission within this structure is spatially limited to the inner edge of the parabolic wall. This may suggest that part of the northern lobe cavity is shielded from

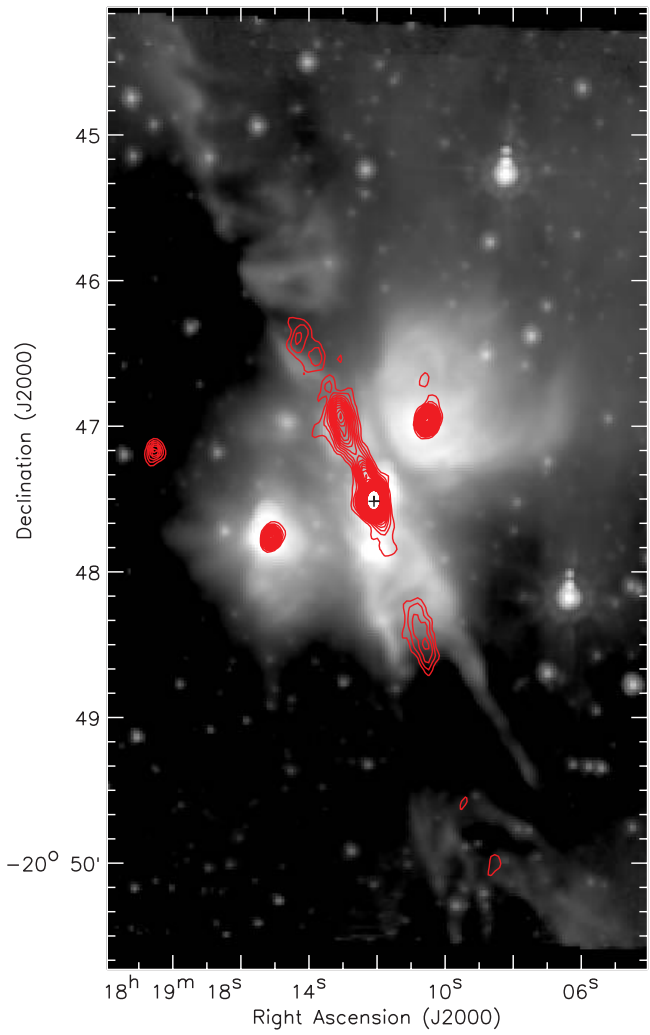

FIG. 10.—HH 80-81: the 8.0 μm band emission in gray scale and the 6 cm continuum emission from Martí et al. (1993) in contours. The plus sign marks the 7 mm continuum peak from Gómez et al. (2003).

the UV photons by gas and dust in the outflow and perhaps by the circumstellar environment around the central source. Two additional reflection nebulae are found on both sides of the bipolar cavity; these appear to be heated by two young B stars (see Table 3) and not directly connected to the outflow cavity.

The central driving source of the outflow has been detected in the centimeter (Martí et al. 1993, 1999) and millimeter (Gómez et al. 2003) continuum. Mid-infrared emission from this source has been detected at 4.7–13 μm in the ground-based observations (Aspin et al. 1994; Stecklum et al. 1997). In Figure 11 the centroid of the emission feature in the 3.6 μm band is about 2″ northeast offset from the millimeter peak. This feature coincides with a *K*-band knot detected in previous ground-based observations (their IRS 2, Aspin et al. 1991, 1994; Stecklum et al. 1997). From its high polarization and relatively large FWHM, Aspin et al. (1991) argued that it is a nebulous knot of gas/dust rather than a point source. The emission feature in the 4.5 μm band shows elongation toward the position of the millimeter peak. The centroid of the emission feature in the 5.8 and 8.0 μm bands, discarding the bandwidth artifact in the north, coincides with the millimeter peak. We suggest that the emission in the 3.6 and 4.5 μm bands is mostly attributed to the IRS 2 knot, while that in the long-wavelength bands is mostly coming from the millimeter core, and their photometry is listed in Table 5. The MIPS

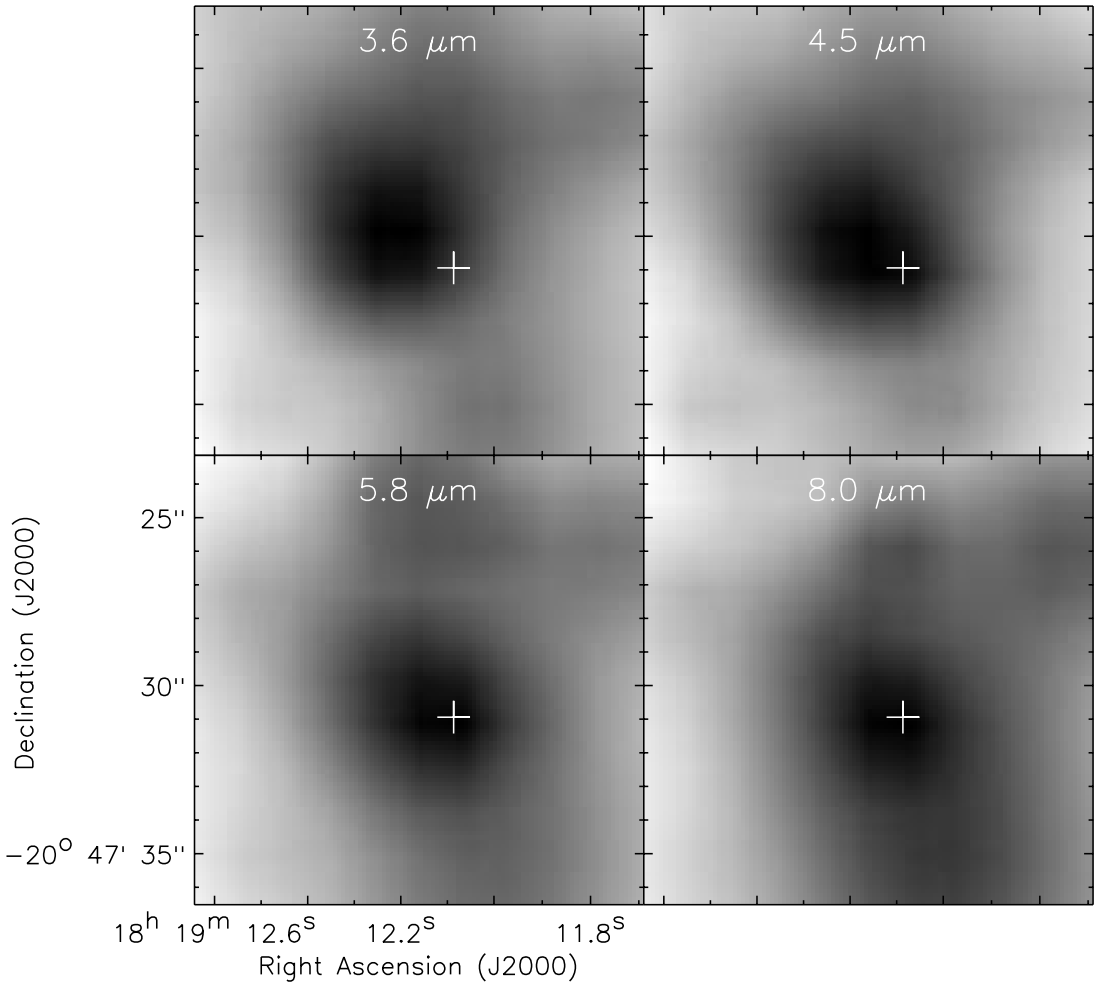

FIG. 11.—HH 80-81: the IRAC band emission from the inner massive star formation site, to show a comparison between the point-source detections in the IRAC bands and previous millimeter continuum observation. The plus sign marks the 7 mm continuum peak from Gómez et al. (2003).

24 μm emission in the central part of this region is significantly saturated.

3.2.5. *IRAS 19410+2336*

As outlined with a dashed ellipse in Figure 12, an elliptical nebula orientated in the northeast-southwest direction can be identified from the extended emission in the central part of IRAS 19410+2336 (hereafter IRAS 19410). In interferometric CO observations, multiple outflows emanating from the center of this region show very complex morphologies (Beuther et al. 2003). The axis of one outflow proposed by Beuther et al., which is shown in contours in Figure 12, coincides with the major axis of the IRAC elliptical nebula. Jetlike 2.12 μm H_2 emission along the axis of this outflow was detected as well (Beuther et al. 2003). The elliptical nebula, with two local cavities at the ends of the major axis, is only detectable in the 3.6 and 4.5 μm bands and appears more prominent in the 3.6 μm band, suggesting the emission is dominated by scattered light from the central source. Apparently the IRAC imaging of the IRAS 19410 outflow reveals a less collimated component than the 2.12 μm H_2 jet.

The driving source of this outflow is suggested to be deeply embedded in a dusty core traced by millimeter continuum emission at a resolution of $5.5'' \times 3.5''$ (Beuther et al. 2003). The infrared emission from this millimeter source is detected in all four IRAC bands and the photometry is listed in Table 5. There is a 2MASS K_s-band detection, with the photometry of

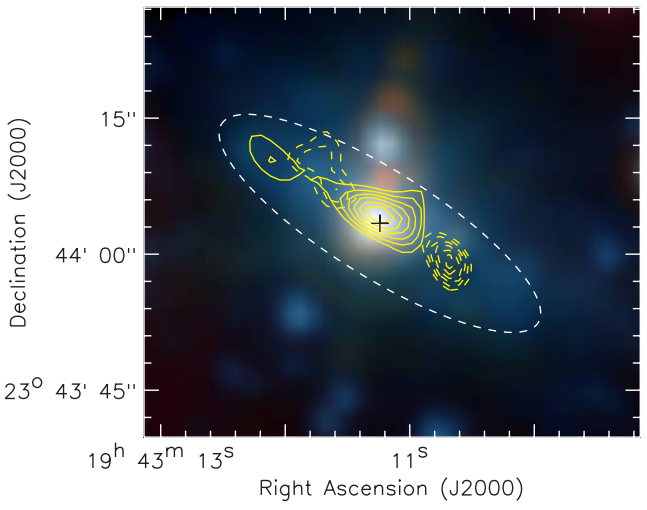

FIG. 12.—IRAS 19410: the 3.6/4.5/8.0 μm three-color composite of the central part. The dashed ellipse outlines the IRAC elliptical structure. Solid and dashed contours show blue- and redshifted lobes from a CO outflow by Beuther et al. (2003), respectively, and the plus sign a millimeter continuum peak therein.

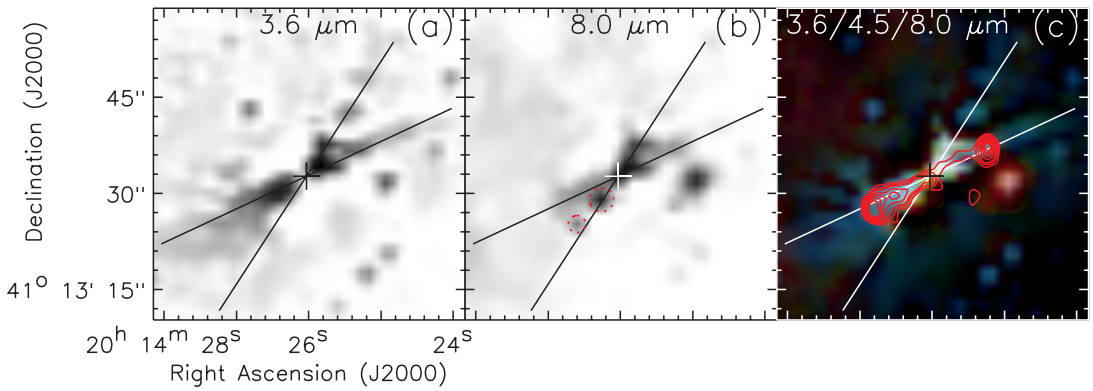

FIG. 13.—IRAS 20126: the IRAC band emission from the central part. (*a*) The 3.6 μm emission. To highlight the bipolar nebula a high-pass filtering in IDL has been applied to the image. (*b*) Same as (*a*), but for the 8.0 μm emission. Infrared emission from the central source is detected at this wavelength. The two dashed circles mark bandwidth artifacts induced by the central bright source. (*c*) The 3.6/4.5/8.0 μm three-color composite, with an SiO (2–1) jet from Cesaroni et al. (1999) overlaid in red contours. In each panel the crossing lines outline the wall of the IRAC biconical structure. The plus sign marks the 1.2 mm continuum peak from Cesaroni et al. (2005).

10.802 ± 0.044, at $\sim 0.7''$ away from the millimeter continuum peak. As we discussed in § 3.2.1, it is more likely another star rather than the infrared counterpart of the millimeter source. The MIPS 24 μm emission from the source is significantly saturated. At a higher resolution ($1.5'' \times 1''$), the millimeter core splits into multiple sources (Beuther & Schilke 2004a); our IRAC observations cannot resolve those sources. A detailed comparison between the IRAC observations and high-spatial-resolution millimeter continuum observations of this region will be presented in a future work (J. A. Rodón et al., in preparation).

3.2.6. *IRAS 20126+4104*

In Figures 13*a* and 13*c* a bipolar outflow in IRAS 20126+4104 (hereafter referred as IRAS 20126) is detected as a limb-brightened biconical cavity. The cavity structure, in particular the wall of the northwestern lobe, is clearly detected in the 3.6, 4.5, and 5.8 μm bands and its prominence in the 3.6 and 4.5 μm bands suggests that the emission is dominated by the scattered light. The molecular outflow in IRAS 20126 has been interpreted as driven by a precessing jet based on the S-shaped locus of the 2.12 μm H_2 knots and the orientation variation between the inner jetlike SiO outflow and the larger CO outflow (Cesaroni et al. 1997, 1999; Shepherd et al. 2000; Lebrón et al. 2006; Su et al. 2007). The jet-precessing scenario is also consistent with the presence of a double system detected at centimeter and near-infrared wavelengths (Sridharan et al. 2005; Hofner et al. 1999, 2007). Our IRAC observations put new insight into the outflow property of this luminous source. The IRAC biconical structure far exceeds inner SiO outflow and covers part of the larger CO outflow. From the limb-brightening, the cavity wall has PAs from $\sim -33^\circ$ to $\sim -65^\circ$. The PA $\sim -33^\circ$ wall is significantly offset from the axis of the larger CO outflow which is nearly in a north-south orientation (Shepherd et al. 2000; Lebrón et al. 2006), while the PA $\sim -65^\circ$ wall has approximately the same orientation as the jetlike SiO outflow. A natural interpretation of the cavity (with the limb-brightening) is that it traces a less collimated biconical component of the IRAS 20126 outflow, rather than being swept up by a jet precessing from north-south to the current position of PA $\sim 33^\circ$. However, in contrast to the HH 80-81 outflow (§ 3.2.4), the jet component in this region coincides with the wall, not the axis, of the biconical cavity. While multiple outflows can be one possibility, another possibility can be derived by adopting the precessing scenario and the theoretical model unifying the jet-driven and wind-driven low-mass outflows (Shang et al. 2007): when the underlying axial jet and the co-existing wind are precessing, the dense jet is more efficient in entraining a collimated molecular outflow via strong shock activities, while the more tenuous wind component is less efficient in evacuating a cavity. Consequently, the jetlike SiO outflow can be detected very close to the current position of the precessing jet while the cavity revealed by the scattered light more or less lags behind.

A dense dusty core, which harbors a proto-B star driving the outflow, was previously detected in the millimeter continuum (Shepherd et al. 2000; Cesaroni et al. 2005). In the 4.5 and 5.8 μm bands the emission feature coincident with the millimeter source is discernible. In the 8.0 μm band (Fig. 13*b*), a point source at this position is detected and the photometry is listed in Table 5. At higher resolutions ($\lesssim 0.5''$), two emission regions oriented along the outflow axis and separated by a dark lane were detected at near- and mid-infrared wavelengths (Sridharan et al. 2005; De Buizer 2007). The source in the 8.0 μm band may encompass the previously detected double sources.

3.2.7. *IRAS 20293+3952*

In Figure 14, ahead of a previously detected high-velocity CO outflow (Beuther et al. 2004b), a short jet is detected in the

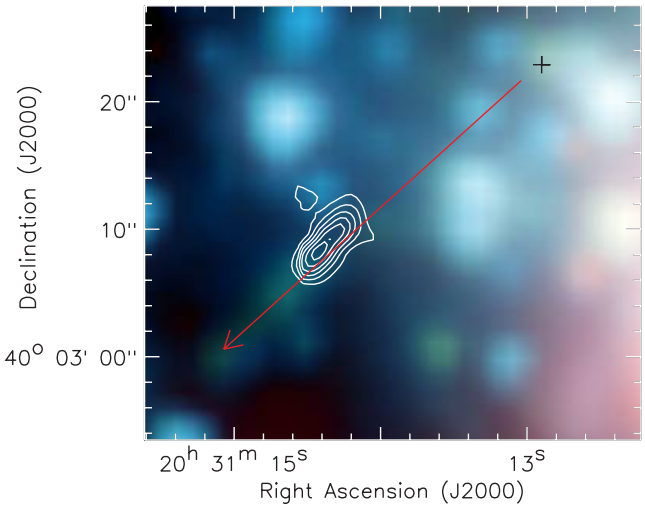

FIG. 14.—IRAS 20293: the 3.6/4.5/8.0 μm three-color composite of the central part. The arrow marks the orientation of a jet prominent in the 4.5 μm band. The contours show blueshifted high-velocity CO emission in a jetlike outflow and the plus sign the millimeter continuum peak from Beuther & Schilke (2004a).

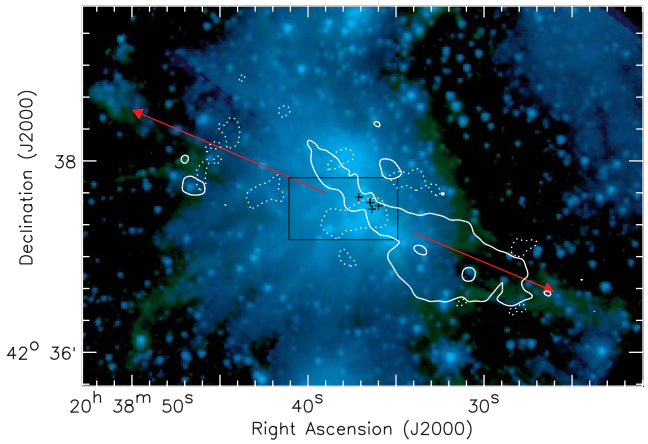

FIG. 15.— W75N: the 3.6/4.5 μm two-color composite of the central part. The double arrows mark the orientation of a large-scale bow-shaped structure. Solid and dashed contours are the lowest contours of red- and blueshifted emission in a CO outflow, respectively (Shepherd et al. 2003). Plus signs mark the millimeter continuum peaks from Shepherd (2001).

IRAC imaging with an extent of about 10″, with the most prominent emission in the 4.5 μm band. In orientation the IRAC jet well coincides with the CO outflow. This outflow was also detected in thermal emissions of SiO and CH_3OH (Beuther et al. 2004b; Palau et al. 2007), which often trace shock activities in outflows. In the previous 2.12 μm H_2 observations, the overall structure was not detected but a faint knot can be found at the southeastern end of the IRAC jet (knot C in Fig. 2 of Kumar et al. 2002). We suggest that the IRAC imaging for the first time reveals the interval driving agent of the CO/SiO/CH_3OH outflow.

A millimeter continuum source, which may harbor an intermediate-mass protostar, is suggested to be the driving source of the CO/SiO/CH_3OH outflow (Beuther et al. 2004b, 2004c; Palau et al. 2007). The infrared emission from the millimeter source is only detected in the MIPS 24 μm band (Table 5). As in the case of AFGL 5142 (§ 3.2.1), the 24 μm detection is located at the bright PSF wing of a nearby saturated source, resulting in a potential overestimate of the source flux by about 0.8–0.9 Jy.

3.2.8. *W75N*

In Figure 15 multiple bow-shaped structures in W75N can be identified. The most remarkable one, marked by the double arrows, forms a large-scale bipolar bow-shaped structure. The shell of the southwestern lobe and the tip of the northeastern lobe of this structure are clearly revealed in the 4.5 μm band. This bow-shaped structure has previously been detected in the 2.12 μm H_2 imaging by several authors (Davis et al. 1998, 2007; Shepherd et al. 2003), but not reported in previous IRAC observations toward the DR 21/W75N region carried out during the science verification period of *Spitzer* (Persi et al. 2006; Davis et al. 2007), probably because their observations are far less deep in integration. The southwestern lobe coincides with the boundary of the redshifted lobe of a large outflow detected in CO (1–0) (Shepherd et al. 2003), suggesting the bow-shock-driven nature of this molecular outflow. In addition to this remarkable structure, at least five bow-shaped structures pointing to the southeast of the region can be found in Figure 15. These structures may be shocked H_2 "fingers" tracing multiple bow shocks driven from the center of the region, roughly in a fashion similar to the famous H_2 fingers in the Orion KL region (Schultz et al. 1999; Nissen et al. 2007). Zooming in on the inner part of this region, the IRAC imaging reveals a new bow-shaped structure (outlined

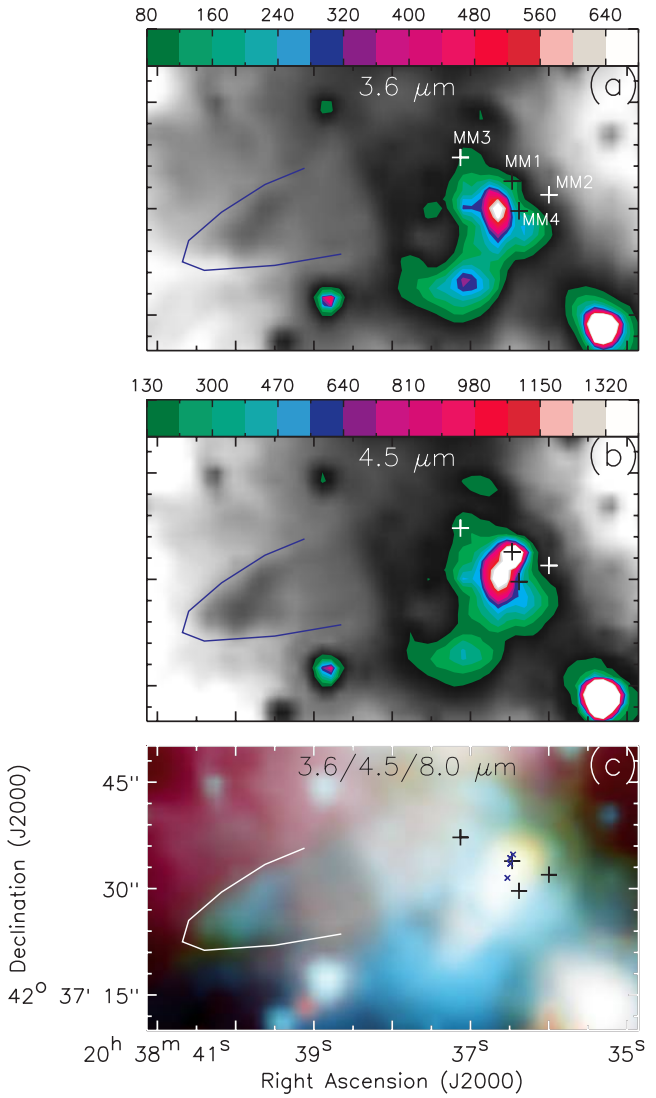

FIG. 16.— W75N: the IRAC band emission of the area labeled as a rectangle in Fig. 15. (*a*) The 3.6 μm emission, with emission levels between 8.2 and 80 MJy sr^{-1} shown in gray scale and that beyond 80 MJy sr^{-1} in colored contours. The contour levels in MJy sr^{-1} are labeled at the top of the image. (*b*) Same as (*a*), but for the 4.5 μm emission. The emission between 10.7 and 130 MJy sr^{-1} is shown in gray scale and that beyond 130 MJy sr^{-1} in colored contours. (*c*) The 3.6/4.5/8.0 μm three-color composite. In each panel a solid curve outlines the edge of a small bow-shaped structure and the plus signs mark the millimeter continuum peaks (MM1–MM4) from Shepherd (2001). The crosses in (*c*) mark the centimeter continuum peaks revealed by Hunter et al. (1995) and Torrelles et al. (1997).

by a solid curve in Fig. 16). This structure is clearly detected in the 3.6 and 4.5 μm bands and appears more prominent in the 4.5 μm band (Figs. 16*a* and 16*b*). Its orientation approximately coincides with the axis of a CO outflow proposed by Shepherd et al. (2003).

At the center of the large northeast-southwest bow-shaped structure, Shepherd (2001) detected a group of four millimeter continuum sources (labeled MM1–MM4 in Fig. 16*a*). Embedded in MM1 is a cluster of four centimeter continuum sources, with three within an area of 1.5″ and another about 3″ to the south (Fig. 16*c*; Hunter et al. 1994; Torrelles et al. 1997; Shepherd et al. 2003). Of the four centimeter sources, the northernmost one was interpreted as an ionized radio jet while the other three were suggested to be UC H II regions excited by proto-B stars. It is still unclear which is driving the large-scale CO outflow. Shepherd et al. (2003) suggested that the first UC H II region from the north

(namely VLA 2) is likely to be the driving source. The resolution of our IRAC observation does not allow us to shed any further light on this issue. Shepherd et al. (2003) suggested that the second UC H II region from the north (namely VLA 3) is the driving source of the CO outflow whose axis approximately coincides with the newly discovered small bow-shaped structure in the IRAC image. However, the CO outflow is very compact and confined to within $\sim 5''$ from MM1 while the bow-shaped structure is about $50''$ (0.5 pc in projection) away from the group of the millimeter sources. In projection MM3 is closer to the axis of this bow-shaped structure and thus more likely to be the driving source of this structure. The infrared emission from MM1 is marginally discernible in the 3.6 μm band (Fig. 16*a*). From 4.5 (Fig. 16*b*) to 8.0 μm it is clearly identified as a point source, and the photometry is listed in Table 5. The MIPS 24 μm emission from the source is significantly saturated.

3.2.9. *IRAS 22172+5912*

IRAS 22172+5912 (hereafter IRAS 22172) is the only region in our sample toward which no outflow signature is found in the IRAC bands, although a bipolar outflow in CO and HCO^+ has been detected with the OVRO array (Molinari et al. 2002; Fontani et al. 2004). The peak of the dust emission, which was detected in the OVRO 2.6 and 3.4 mm continuum observations at $\sim 4''$–$6''$ resolutions, is about $5''$ offset from the geometric center of the bipolar molecular outflow (Molinari et al. 2002; Fontani et al. 2004). The IRAC and MIPS 24 μm imaging does not detect infrared emission from the millimeter source but reveals two protostars at the center of this field (see Fig. 2*i*). The southern protostar coincides with the geometric center of the CO outflow and thus can be a candidate for the driving source of the outflow. For the millimeter source, the lack of infrared emission shortward of 24 μm and the apparent nonassociation with the molecular outflow suggest that the source is at a very young evolutionary stage. Further (sub)millimeter continuum and line observations with high sensitivity and higher resolutions are needed to verify whether it is at a prestellar stage or harbors deeply embedded protostars.

3.3. *UV Heated Reflection Nebulae and Bright Rimmed Clouds*

The IRAC imaging of the sample reveals mainly three classes of extended emission: H_2 emission dominated nebulae most prominent in the 4.5 μm band (*green*); scattered light dominated nebulae most prominent in the 3.6 μm band (*blue*); and UV heated hydrocarbon emission dominated reflection nebulae most prominent in the 8.0 μm band (*red*). The first two classes have been discussed in detail in § 3.2.

The UV-heated reflection nebulae can be found in most regions. While the first two classes of extended emission are found in outflows or outflow cavities and thus imply a very young evolutionary stage of the central source, most of the UV-heated reflection nebulae are associated with young but relatively more evolved B stars (one exception being the biconical cavity of the HH 80-81 outflow). For the cometary nebula in AFGL 5142, the southwestern nebula in IRAS 05358, the southeastern and northwestern nebulae in HH 80-81, the central nebula in IRAS 20293, and the northern and central nebulae in W75N, a bright source at the center is detected (denoted as a blue cross in Fig. 2). These sources show infrared excess in our census of YSOs based on color-color diagrams, and most of them were previously suggested to be intermediate- to high-mass young stars (see annotation of Table 3). They are most likely the exciting sources of the surrounding reflection nebulae. Of these sources, the one in IRAS 20293 shows an UC H II region and the central one in W75N is surrounded by a relatively extended H II region. The spectral types of the exciting stars of these two H II regions, derived from the Lyman continuum photos required to produce the observed ionized emission, are B1 and B0.5 for that in IRAS 20293 and W75N, respectively (Palau et al. 2007; Shepherd et al. 2004b). Toward the two sources in HH 80-81, compact centimeter continuum was detected as well (Martí et al. 1993), and the estimated rates of Lyman continuum photos suggest B3–B2 stars being the exciting sources of these two reflection nebulae. There is no reported detection of a distinct H II region surrounding the other candidate exciting sources. We suggest that they are young B stars capable of providing FUV radiation strong enough to excite hydrocarbon emission but EUV too weak to ionize its environment. Spectroscopic studies are needed to further investigate whether these stars have circumstellar disks and to confirm their spectral types. There are also UV-heated reflection nebulae for which an exciting source cannot be identified with the existing data, but the need of FUV photons to heat hydrocarbons and the lack of significant free-free emission also suggest a B-type star being the exciting source. To lower the optical depth in FUV and consequently allow the stars to heat the surrounding hydrocarbons, these B stars must have cleared most of the surrounding gas. On the other hand, as discussed in § 3.2, the central massive star formation site in each region shows millimeter continuum cores harboring deeply imbedded proto-B stars. Thus it appears that most regions in the sample are forming B stars at a range of evolutionary stages.

In two regions, IRAS 20126 and IRAS 22172, the central massive star formation sites are embedded in a bright large-scale structure which is prominent in the 8.0 μm band. These two structures are externally heated rimmed clouds.

4. DISCUSSION

4.1. *Clustering*

One of the distinctive features of massive star formation is that it occurs in clusters. Consequently, understanding the role of clustering in the formation of high-mass stars is an essential step toward a theory of massive star formation. A controversial issue is whether clusters are necessary for the formation of high-mass stars, or whether clusters are merely the by-product of the formation of high-mass stars in dense massive molecular cores. In a near-infrared survey of intermediate-mass Herbig Ae/Be stars, Testi et al. (1999) found a smooth transition between the low-density aggregates of young stars associated with stars of spectral type A or later, and the dense clusters associated with O and early-B type stars. They argued that the presence of dense clusters is required for the formation of high-mass stars. The smooth transition suggested that there may be a fundamental relationship between the mass of the most massive star and the number and/or density of stars in a cluster. However, de Wit et al. (2005) found evidence that 4% of O stars form in isolation. This is evidence that clusters are not necessary for the formation of O stars, although Parker & Goodwin (2007) argued that the isolated O stars may actually form in small clusters.

To test whether massive stars can form without low-mass stars requires identification of young massive objects without associated clusters of low-mass stars; only in these cases can we rule out the possibility that an attendant cluster dispersed due to dynamical evolution. In a *K*-band survey of eight high-mass star forming cores, Sollins & Megeath (2004) found one core, NGC 6334I(N), showing evidence of high-mass star formation without evidence for a cluster of embedded low-mass stars (also see Megeath & Tieftrunk 1999; Hunter et al. 2006), although a

cluster may still exist deeply embedded in the cloud (Persi et al. 2005). It is important to search for other potential examples of massive star formation without the presence of a dense cluster. With its ability to identify YSOs through infrared excesses and detect deeply embedded protostars, *Spitzer* is well suited to this task. Although such regions may yet form clusters, the identification of high-mass young or protostars without a dense cluster would demonstrate that low-mass stars are not required for the formation of massive stars.

Our survey of young intermediate- to high-mass (proto)stars ($\sim 10^3$–$10^5\ L_\odot$) can directly address the role of clustering in the early stages of intermediate- and high-mass forming stars. The *Spitzer* data provide the ability to directly identify likely YSOs by the detection of mid-infrared excesses. The advantage of this approach over previous near-infrared source counting methods is that the sample does not significantly suffer from contamination by background stars which can be significant for high-mass star forming regions in the Galactic plane (Pratap et al. 1999). Also, the mid-infrared colors are much more sensitive to protostellar objects, and candidate protostellar objects can be identified through their colors. However, the bright mid-infrared nebulosity in high-mass star forming regions, the $\sim 2''$–$3''$ angular resolution of the IRAC data, and the modest sensitivity of the 2MASS photometry limit the detection of sources, in particular in regions of bright nebulosity. We expect the census of YSOs to be incomplete in all of the regions. Furthermore, we expect that a certain fraction of the stars do not have disks and will not be identified in our analysis; the fraction of stars without disks is approximately 30% for 1 Myr old low-mass stars (Hernández et al. 2007).

We group the objects by their total far-infrared luminosity, as measured from the *IRAS* point-source catalog; this luminosity will be dominated by the most massive objects in the regions. In all the regions, associated low-mass YSOs are detected. The $\sim 10^3\ L_\odot$ regions, AFGL 5142, G192, IRAS 05358, and IRAS 20293, show parsec-sized clusters with around 20 YSOs surrounded by a more extended and sparse distribution of young stars and protostars. The $\sim 10^4\ L_\odot$ regions IRAS 19410 and HH 80-81 also show clusters and extended components. Except for AFGL 5142, the clusters associated with these regions do not show concentrations of stars toward the central massive objects. This may be due to the decrease in completeness toward the bright nebulosities in the central regions. Finally, the $10^{5.1}\ L_\odot$ region W75N shows a cluster that is both richer and more spatially extended. This region also shows a paucity of sources in the bright nebulous center of the region, further indicating that the observations are significantly limited by incompleteness.

In Figure 17 we plot the number of sources as a function of the source luminosity. To mitigate the effects of incompleteness on our samples, we plot the number of sources with 3.6 μm magnitudes lower than 13 and 14. Given a typical $K_s - [3.6]$ color of 0.25, an extinction of $A_K \sim 0.25$ at 1.8 kpc, and an age of 1 Myr, these limits correspond to masses of 1.2 and 0.5 $M_\odot$ (Baraffe et al. 1998). The two plots show a trend of increasing number of associated YSOs with increasing total luminosity. In particular, the number of YSOs in the $10^{5.1}\ L_\odot$ region (W75N) is significantly higher than those in $\sim 10^4\ L_\odot$ regions, which again are somewhat higher in number than the $\sim 10^3\ L_\odot$ regions. It is possible that a trend of increasing incompleteness with higher far-infrared luminosities is decreasing the slope of this trend.

There are two main exceptions to this trend: IRAS 22172 and IRAS 20126. IRAS 22172 appears to be part of a larger, potentially more evolved region which has undergone significant gas clearing. The clearing of the gas would also lower the fraction of light absorbed by dust and re-emitted in the infrared; hence this region shows a large number of stars for its measured IRAS far-infrared luminosity. The other exception is IRAS 20126, which has the lowest number of associated YSOs in the sample. Unlike the other regions, IRAS 20126 shows no obvious cluster in the field. This is unlikely to be solely the effect of incompleteness, with the average signal of about 2.5 MJy sr^{-1} at 4.5 μm and 52 MJy sr^{-1} at 8.0 μm in the central parsec area, compared to 6.5 MJy sr^{-1} at 4.5 μm and 67 MJy sr^{-1} at 8.0 μm for HH 80-81 and 3.8 MJy sr^{-1} at 4.5 μm and 72 MJy sr^{-1} at 8.0 μm for IRAS 19410.

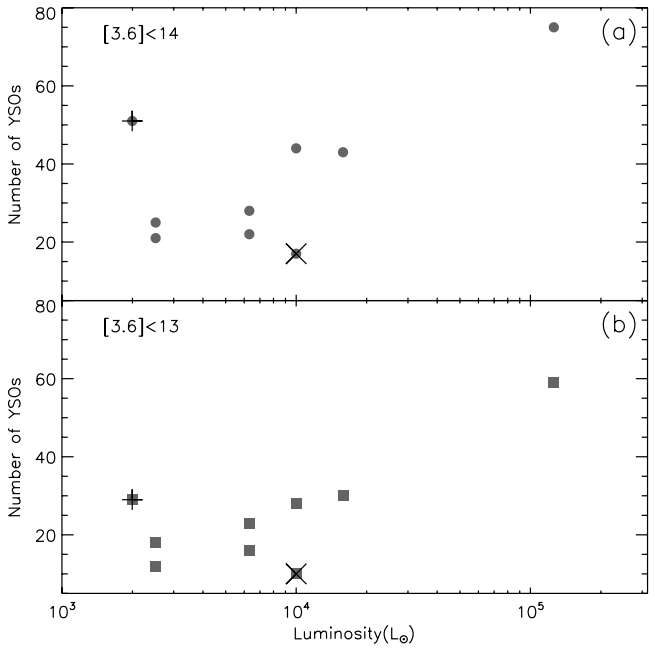

FIG. 17.—The number of detected YSOs vs. the IRAS luminosity. (*a*) The number of YSOs counted from those with $[3.6] < 14$. The data points for IRAS 22172 and IRAS 20126 are overlaid with a plus sign and a cross, respectively. (*b*) Same as (*a*), but for YSOs with $[3.6] < 13$.

More rigorous studies of this sample await deeper near-infrared data to complement the *Spitzer* 3.6 and 4.5 μm imaging. However, the analysis here already illustrates several features. First, there does seem to be a trend of the number of associated YSOs with luminosity. Second, these regions show both clusters in the central 1 pc as well as more extended halos of sources around the clusters. Finally, there does seem to be a significant dispersion in the number of associated YSOs for a given total far-infrared luminosity, with one luminous source, IRAS 20126, showing no obvious cluster. The lack of a cluster warrants future work; if confirmed this would demonstrate that the formation of $\sim 10^4\ L_\odot$ sources is not dependent on the presence of deep clusters.

4.2. *Outflows and Outflow Cavities*

For a sample of nine high-mass star forming regions associated with CO and/or SiO outflows, the deep IRAC imaging reveals outflows and outflow cavities toward eight regions, illustrating that the IRAC imaging can be an effective tool for outflow detection. For the jets in IRAS 05358, AFGL 5142, and IRAS 20293, the bow shock shells in W75N, and the nebulosities in the eastern lobe of the G192 outflow, the prominence in the 4.5 μm band and coincidence with the ground-based 2.12 μm H_2 detections (if detected in the 2.12 μm H_2 line) suggest that the emission can mostly be attributed to shocked H_2 emission, although the contribution from H I Brα (4.052 μm), CO $v = 1$–0 (4.45–4.95 μm) lines cannot be ruled out without spectroscopic

observations. A detailed investigation of the emission in the biconical cavity in IRAS 20126 shows strong evidence for the scattered light being dominant in the 3.6 and 4.5 μm bands (K. Qiu et al., in preparation). The elliptical structure in IRAS 19410 appears relatively diffuse and most prominent in the 3.6 μm band. The emission in this outflow can be dominated by the scattered light as well. The clear prominence of the biconical structure in HH 80-81 that is suggested is dominated by UV-heated hydrocarbon emission.

4.2.1. *An Evolutionary Picture of Massive Outflows?*

Both theoretical models and high-spatial-resolution observations suggest an evolutionary scenario for low-mass outflows: as low-mass stars evolve from Class 0 through Class I to Class II stages, the mass loading in the winds and density structure in the cores conspire to produce the widening of outflows (Fuller & Ladd 2002; Arce & Sargent 2006; Shang et al. 2007), while for massive outflows, whether or not an evolutionary picture exists is unknown (Beuther & Shepherd 2005).

The detected outflows in the sample show dramatically different morphologies. We detect highly collimated jets, bow shock shells, and biconical cavities. Given the extreme complexity of the CO observations (Beuther et al. 2003) and relatively confused emission in the IRAC imaging compared with the other regions, we leave out the IRAS 19410 outflow in the following discussion. Considering jet 1 in IRAS 05358, the short jet in AFGL 5142, and the jet in IRAS 20293, the IRAC observations reveal the internal driving agents of well-collimated CO outflows in these regions. The powering sources of jet 1 in IRAS 05358 and the short jet in AFGL 5142 are suggested to be deeply embedded proto-B stars, toward which only very weak radio continuum was detected (Beuther et al. 2007; Zhang et al. 2007). The jet in IRAS 20293 is most likely driven by an intermediate-mass protostar showing no detectable centimeter emission (Beuther et al. 2004b). In contrast, the large-scale CO outflows in W75N and G192 appear to be poorly collimated within $\lesssim$0.5 pc from the central driving sources. In W75N, proper-motion observations of water masers by Torrelles et al. (2003) delineated a noncollimated shell outflow at a 160 AU scale expanding in multiple directions with respect to the UC H II region VLA 2, which may drive the large-scale CO outflow, as suggested by Shepherd et al. (2003). The bipolar bow-shaped structure beyond $\sim$1 pc detected in the 2.12 μm H_2 and the IRAC 4.5 μm imaging could be the remnant of a collimated component. For the G192 outflow, no collimated component can be found within $\sim$2.4 pc from the driving source. The proposed central driving sources of these two poorly collimated outflows are found to be surrounded by UC H II regions. If we adopt the centimeter free-free emission as an indicator of the relative evolution between these sources, there seems to be a trend of evolution for the related outflows: both internal driving agents and entrained molecular outflows appear to be highly collimated for the youngest sources (e.g., IRAS 05358, AFGL 5142, IRAS 20293); as the central source evolves to form a significant UC H II region, only poorly collimated outflow structures can be found around the central driving source (e.g., W75N, G192).

For the IRAS 20126 outflow, it remains ambiguous whether it is merely composed of a precessing jet and consequently larger structures are all entrained/swept up by this jet or whether it has a jetlike component as well as a biconical component with a moderate opening angle. Toward the central driving source of this outflow, very weak centimeter continuum was detected, presumably suggesting that the source is at a very young evolutionary stage. For the HH 80-81 outflow, our *Spitzer* data and previous centimeter continuum reveal a remarkable two-component outflow with a biconical cavity surrounding an axial radio jet. Strong centimeter continuum was detected toward the central driving source of the HH 80-81 outflow, presumably suggesting that the source is relatively more evolved compared with that of IRAS 20126. The outflow cavity of HH 80-81 also shows emission in the mid-infrared hydrocarbon features, suggesting that UV radiation from the central sources is heating the cavity walls. Therefore, if the IRAC biconical cavity in IRAS 20126 is a complementary, less-collimated component of the previously detected SiO jet, there will be a large evolutionary timescale for the existence of both a highly collimated jetlike component and a less collimated biconical component for outflows from proto-B stars. With the existing data it is very difficult to determine whether the central source of IRAS 20126 is more evolved than those of AFGL 5142 and IRAS 05358, and whether the central source of HH 80-81 is younger than those of W75N and G192. Presumably it is likely that the IRAS 20126 and HH 80-81 outflows, with the former being younger, represent evolutionary stages between that of the AFGL 5142 and IRAS 05358 outflows, for which both internal driving agents and entrained gas appear well collimated, and that of the W75N and G192 outflows, for which only poorly collimated structures can be found around the central driving sources.

However, such a trend is only a tentative interpretation based on current observations of a small sample. The question of whether there is an evolutionary picture for massive outflows is far from conclusive, and remains an observational challenge. In high-mass star forming regions, multiple outflows with complicated structures are often detected. Due to relatively larger distances and the crowded clustering mode, it is very difficult with the current facilities to reliably identify the driving source of a massive outflow. Also, resolving the launching zone of a massive outflow, which is of great importance for investigate driving mechanisms, requires extremely high spatial resolution and high sensitivity. In addition, observations of outflows in more luminous objects ($L \gtrsim 10^5\ L_\odot$), in particular high-spatial-resolution observations, are still rare (the combined bolometric luminosity of UC H II regions in MM1 in W75N is $10^{4.6}\ L_\odot$). Extensive and comprehensive studies of outflows in this luminosity regime would be crucial for testing possible evolutionary scenarios of massive outflows and understanding formation processes of O-type stars.

5. SUMMARY

We have described initial results of mid-infrared imaging observations toward nine high-mass star forming regions made with the IRAC and MIPS cameras on board *Spitzer*. The regions were selected for the presence of luminous ($>10^3\ L_\odot$) young objects driving molecular outflows. The observed fields are approximately $5' \times 5'$, corresponding to physical widths of $\sim$2.5–3.5 pc for the source distances ranging from $\sim$1.7 to 2.4 kpc.

Using the 3–24 μm *Spitzer* photometry in combination with near-infrared 2MASS data, we identify a total of 417 YSOs with infrared excesses attributed to circumstellar disks or envelopes, including at least 12 candidates of intermediate- to high-mass young stars. In most regions, the spatial distribution of these YSOs shows both a cluster component centered on the sites of massive star formation as well as a more extended distribution of YSOs outside the cluster. The number of YSOs grows with the total far-infrared luminosity, with two significant exceptions: IRAS 22172 appears to be part of a larger, more evolved region; IRAS 20126 appears to be a $10^4\ L_\odot$ protostar with only 19 associated YSOs and no central cluster.

Zooming in on the central massive star formation sites, we search for infrared counterparts toward millimeter continuum sources identified in interferometer observations. We detected counterparts for eight millimeter continuum sources in the IRAC bands or MIPS 24 μm band. These eight sources appear to be natal cores of proto-B stars driving molecular outflows. All of the regions of massive star formation have bright associated nebulosity from scattered light and shocked H_2 and/or UV heated hydrocarbon emission features. This nebulosity limits the completeness of our YSO survey in the central areas.

The deep IRAC imaging detects features associated with 12 outflows in eight of the surveyed regions. Compared with previous ground-based observations, our IRAC observations confirm previous 2.12 μm H_2 jets or bow-shock-shaped structures in AFGL 5142, IRAS 05358, and W75N (the large bow-shock-shaped structure) and previous Hα/[S II] features in G192; reveal new structures in HH 80-81, IRAS 20126, and IRAS 19410; and detect a new H_2 jet in IRAS 20293 and a new bow-shock-shaped structure in W75N (the small bow-shock-shaped structure). In one case, HH 80-81, the inner surface of the outflow cavity shows strong 8 μm emission indicative of hydrocarbons heated by UV radiation. Based on the morphological variations of the detected outflows in conjunction with previous observations, we outline a possible evolutionary picture for massive outflows.

UV-heated reflection nebulae dominated by hydrocarbon emission in the 8.0 μm band can be found in most regions. They may imply the presence of relatively more evolved young B stars. Externally heated bright rimmed clouds are found in IRAS 20126 and IRAS 22172.

We are grateful to Luis F. Rodríguez for providing us the VLA cm data on HH 80-81. This work is based on observations made with the *Spitzer Space Telescope*, which is operated by the Jet Propulsion Laboratory, California Institute of Technology under a contract with the National Aeronautics and Space Administration (NASA). This publication makes use of data products from the Two Micron All Sky Survey, which is a joint project of the University of Massachusetts and the Infrared Processing and Analysis Center/California Institute of Technology, funded by NASA and the National Science Foundation. K. Q. acknowledges the support of grant 10128306 from NSFC. H. B. acknowledges financial support by the Emmy Noether Program of the Deutsche Forschungsgemeinschaft (DFG, grant BE2578).

REFERENCES

Allen, L. E., et al. 2004, ApJS, 154, 363
Arce, H. G., & Sargent, A. I. 2006, ApJ, 646, 1070
Aspin, C., & Geballe, T. R. 1992, A&A, 266, 219
Aspin, C., McCaughrean, M. J., Casali, M. M., & Geballe, T. R. 1991, A&A, 252, 299
Aspin, C., et al. 1994, A&A, 292, L9
Baraffe, I., Chabrier, G., Allard, F., & Hauschildt, P. H. 1998, A&A, 337, 403
Benedettini, M., Molinari, S., Testi, L., & Noriega-Crespo, A. 2004, MNRAS, 347, 295
Beuther, H., Leurini, S., Schike, P., Wyrowski, F., Menten, K. M., & Zhang, Q. 2007, A&A, 466, 1065
Beuther, H., & Schilke, P. 2004a, Science, 303, 1167
Beuther, H., Schike, P., & Gueth, F. 2004b, ApJ, 608, 330
Beuther, H., Schike, P., Gueth, F., McCaughrean, M., Andersen, M., Sridharan, T. K., & Menten, K. M. 2002, A&A, 387, 931
Beuther, H., Schike, P., & Stanke, T. 2003, A&A, 408, 601
Beuther, H., Schike, P., & Wyrowski, F. 2004c, ApJ, 615, 832
Beuther, H., & Shepherd, D. S. 2005, in Cores to Clusters: Star Formation with Next Generation Telescopes, ed. M. S. N. Kumar et al. (New York: Springer), 105
Calvet, N., Hartmann, L., Kenyon, S. J., & Whitney, B. A. 1994, ApJ, 434, 330
Cesaroni, R., Felli, M., Jenness, T., Neri, R., Olmi, L., Robberto, M., Testi, L., & Walmsley, C. M. 1999, A&A, 345, 949
Cesaroni, R., Felli, M., Testi, L., Walmsley, C. M., & Olmi, L. 1997, A&A, 325, 725
Cesaroni, R., Neri, R., Olmi, L., Testi, L., Walmsley, C. M., & Hofner, P. 2005, A&A, 434, 1039
Chen, Y., Yao, Y., Yang, J., & Zeng, Q. 2005, ApJ, 629, 288
Davis, C. J., Kumar, M. S. N., Sandell, G., Froebrich, D., Smith, M. D., & Currie, M. J. 2007, MNRAS, 374, 29
Davis, C. J., Smith, M. D., & Moriarty-Schieven, G. H. 1998, MNRAS, 299, 825
De Buizer, J. M. 2007, ApJ, 654, L147
Devine, D., Bally, J., Reipurth, B., Shepherd, D., & Watson, A. 1999, AJ, 117, 2919
de Wit, W. J., Testi, L., Palla, F., & Zinnecker, H. 2005, A&A, 437, 247
Fazio, G. G., et al. 2004, ApJS, 154, 10
Flaherty, K. M., Pipher, J. L., Megeath, S. T., Winston, E. M., Gutermuth, R. A., Muzerolle, J., Allen, L. E., & Fazio, G. G. 2007, ApJ, 663, 1069
Fontani, F., Cesanori, R., Testi, L., Molinari, S., Zhang, Q., Brand, J., & Walmsley, C. M. 2004, A&A, 424, 179
Fuller, G. A., & Ladd, E. F. 2002, ApJ, 573, 699
Gómez, Y., Rodríguez, L. F., Girart, J. M., Garay, G., & Martí, J. 2003, ApJ, 597, 414
Greene, T. P., Wilking, B. A., André, P., Young, E. T., & Lada, C. J. 1994, ApJ, 434, 614
Gutermuth, R. A., Megeath, S. T., Muzerolle, J. M., Allen, L. E., Pipher, J. L., Myers, P. C., & Fazio, G. G. 2004, ApJS, 154, 374
Gutermuth, R. A., Megeath, S. T., Pipher, J. L., Williams, J. P., Allen, L. E., Myers, P. C., & Raines, N. 2005, ApJ, 632, 397
Gutermuth, R. A., et al. 2008, ApJ, 674, 336
Hartmann, L., Megeath, S. T., Allen, L., Luhman, K., Calvet, N., D'Alessio, P., Franco-Hernandez, R., & Fazio, G. 2005, ApJ, 629, 881
Haschick, A. D., Reid, M. J., Burke, B. F., Moran, J. M., & Miller, G. 1981, ApJ, 244, 76
Hatchell, J., Fuller, G. A., Richer, J. S., Harries, T. J., & Ladd, E. F. 2007, A&A, 468, 1009
Hernández, J., et al. 2007, ApJ, 662, 1067
Hofner, P., Cesaroni, R., Olmi, L., Rodríguez, L. F., Martí, J., & Araya, E. 2007, A&A, 465, 197
Hofner, P., Cesaroni, R., Rodríguez, L. F., & Martí, J. 1999, A&A, 345, L43
Hora, J. L., et al. 2004, Proc. SPIE, 5487, 77
Hunter, T. R., Brogan, C. L., Megeath, S. T., Menten, K. M., Beuther, H., & Thorwirth, S. 2006, ApJ, 649, 888
Hunter, T. R., Taylor, G. B., Felli, M., & Tofani, G. 1994, A&A, 284, 215
Hunter, T. R., Testi, L., Taylor, G. B., Tofani, G., Felli, M., & Phillips, T. G. 1995, A&A, 302, 249
Jiang, Z., Yao, Y., Yang, J., Ishii, M., Nagata, T., Nakaya, H., & Sato, S. 2001, AJ, 122, 313
Kumar, M. S. N., Bachiller, R., & Davis, C. J. 2002, ApJ, 576, 313
Kumar, M. S. N., & Grave, J. M. C. 2007, A&A, 472, 155
Kumar, M. S. N., Keto, E., & Clerkin, E. 2006, A&A, 449, 1033
Lada, C. J., & Lada, E. A. 2003, ARA&A, 41, 57
Lebrón, M., Beuther, H., Schike, P., & Stanke, Th. 2006, A&A, 448, 1037
Lee, C.-F., Ho, P. T. P., Beuther, H., Bourke, T. L., Zhang, Q., Hirano, N., & Shang, H. 2006, ApJ, 639, 292
Longmore, S. N., Burton, M. G., Minier, V., & Walsh, A. J. 2006, MNRAS, 369, 1196
Martí, J., Rodgríguez, L. F., & Reipurth, B. 1993, ApJ, 416, 208
———. 1995, ApJ, 449, 184
———. 1998, ApJ, 502, 337
Martí, J., Rodgríguez, L. F., & Torrelles, J. M. 1999, A&A, 345, L5
Megeath, S. T., & Tieftrunk, A. R. 1999, ApJ, 526, L113
Megeath, S. T., et al. 2004, ApJS, 154, 367
Molinari, S., Testi, L., Rodríguez, L. F., & Zhang, Q. 2002, ApJ, 570, 758
Moore, T. J. T., Mountain, C. M., & Yamashita, T. 1991, MNRAS, 248, 79
Muzerolle, J., et al. 2004, ApJS, 154, 379
Nissen, H. D., Gustafsson, M., Lemaire, J. L., Clénet, Y., Rouan, D., & Field, D. 2007, A&A, 466, 949
Noriega-Crespo, A., Moro-Martin, A., Carey, S., Morris, P. W., Padgett, D. L., Latter, W. B., & Muzerolle, J. 2004a, ApJS, 154, 402
Noriega-Crespo, A., et al. 2004b, ApJS, 154, 352
Palau, A., Estalella, R., Girart, J. M., Ho, P. T. P., Zhang, Q., & Beuther, H. 2007, A&A, 465, 219

Palau, A., et al. 2006, ApJ, 636, L137
Parker, R. J., & Goodwin, S. P. 2007, MNRAS, 380, 1271
Persi, P., Tapia, M., Roth, M., Gómez, M., & Marenzi, A. R. 2005, in IAU Symp. 227, Massive Star Birth: A Crossroads of Astrophysics, ed. R. Cesaroni et al. (Cambridge: Cambridge Univ. Press), 291
Persi, P., Tapia, M., & Smith, H. A. 2006, A&A, 445, 971
Pipher, J. L., et al. 2004, Proc. SPIE, 5487, 234
Porras, A., Cruz-González, I., & Salas, L. 2000, A&A, 361, 660
Pratap, P., Megeath, S. T., & Bergin, E. A. 1999, ApJ, 517, 799
Raga, A. C., Noriega-Crespo, A., González, R. F., & Velázquez, P. F. 2004, ApJS, 154, 346
Reach, W. T., et al. 2005, PASP, 117, 978
Rieke, G. H., et al. 2004, ApJS, 154, 25
Rho, J., Reach, W. T., Lefloch, B., & Fazio, G. G. 2006, ApJ, 643, 965
Robitaille, T. P., Whitney, B. A., Indebetouw, R., Wood, K., & Denzmore, P. 2006, ApJS, 167, 256
Schultz, A. S. B., Colgan, S. W. J., Erickson, E. F., Kaufman, M. J., Hollenbach, D. J., O'dell, C. R., Young, E. T., & Chen, H. 1999, ApJ, 511, 282
Shang, H., Li, Z.-Y., & Hirano, N. 2007, in Protostars and Planets V, ed. B. Reipurth, D. Jewitt, & K. Keil (Tucson: Univ. Arizona Press), 261
Shepherd, D. S. 2001, ApJ, 546, 345
Shepherd, D. S., Borders, T., Claussen, M., Shirley, Y., & Kurtz, S. 2004a, ApJ, 614, 211
Shepherd, D. S., & Kurtz, S. E. 1999, ApJ, 523, 690
Shepherd, D. S., Kurtz, S. E., & Testi, L. 2004b, ApJ, 601, 952
Shepherd, D. S., Testi, L., & Stark, D. P. 2003, ApJ, 584, 882
Shepherd, D. S., Watson, A. M., Sargent, A. I., & Churchwell, E. 1998, ApJ, 507, 861
Shepherd, D. S., Yu, K. C., Bally, J., & Testi, L. 2000, ApJ, 535, 833
Smith, H. A., Hora, J. L., & Marengo, M. 2006, ApJ, 645, 1264
Smith, M. D., & Rosen, A. 2005, MNRAS, 357, 1370
Sollins, P. K., & Megeath, S. T. 2004, AJ, 128, 2374
Sridharan, T. K., Williams, S. J., & Fuller, G. A. 2005, ApJ, 631, L73
Stecklum, B., Feldt, M., Richichi, A., Calamai, G., & Lagage, P. O. 1997, ApJ, 479, 339
Stern, D., et al. 2005, ApJ, 631, 163
Su, Y. N., Liu, S.-Y., Chen, H.-R., Zhang, Q., & Cesaroni, R. 2007, ApJ, 671, 571
Testi, L., Palla, F., & Natta, A. 1999, A&A, 342, 515
Tobin, J. L., Looney, L. W., Mundy, L. G., Kwon, W., & Hamidouche, M. 2007, ApJ, 659, 1404
Torrelles, J. M., Gómez, J. F., Rodríguez, L. F., Ho, P. T. P., Curiel, S., & Vázquez, R. 1997, ApJ, 489, 744
Torrelles, J. M., et al. 2003, ApJ, 598, L115
van den Ancker, M. E., Tielens, A. G. G. M., & Wesselius, P. R. 2000, A&A, 358, 1035
Velusamy, T., Langer, W. D., & Marsh, K. A. 2007, ApJ, 668, L159
Walther, D. M., Aspin, C., & McLean, I. S. 1990, ApJ, 356, 544
Werner, M. W., Uchida, K. I., Marengo, M., Gordon, K. D., Morris, P. W., Houck, J. R., & Stansberry, J. A. 2004, ApJS, 154, 309
Whitney, B. A., Wood, K., Bjorkman, J. E., & Cohen, M. 2003, ApJ, 598, 1079
Whitney, B. A., et al. 2004, ApJS, 154, 315
Winston, E., et al. 2007, ApJ, 669, 493
Yamashita, T., Suzuki, H., Kaifu, N., & Tamura, M. 1989, ApJ, 347, 894
Zhang, Q., Hunter, T. R., Beuther, H., Sridharan, T. K., Liu, S.-Y., Su, Y.-N., Chen, H.-R., & Chen, Y. 2007, ApJ, 658, 1152